

Portland State University

PDXScholar

Geology Faculty Publications and Presentations

Geology

8-2021

Insight Into the Early Exhumation of the Cycladic Blueschist Unit, Syros, Greece: Combined Application of Zoned Garnet Geochronology, Thermodynamic Modeling, and Quartz Elastic Barometry

Jennifer S. Gorce
Virginia Tech

Mark J. Caddick
Virginia Tech

Ethan F. Baxter
Boston College

Besim Dragovic

University of South Carolina works at: https://pdxscholar.library.pdx.edu/geology_fac



Part of the Geology Commons

J. C. Schumacher
jcs7@pdx.edu

Let us know how access to this document benefits you.

Citation Details *for additional authors*

Gorce, J. S., Caddick, M. J., Baxter, E. F., Dragovic, B., Schumacher, J. C., Bodnar, R. J., & Kendall, J. F. (2021). Insight into the early exhumation of the Cycladic Blueschist Unit, Syros, Greece: Combined application of zoned garnet geochronology, thermodynamic modeling, and quartz elastic barometry. *Geochemistry, Geophysics, Geosystems*, 22, e2021GC009716. <https://doi.org/10.1029/2021GC009716>

This Article is brought to you for free and open access. It has been accepted for inclusion in Geology Faculty Publications and Presentations by an authorized administrator of PDXScholar. Please contact us if we can make this document more accessible: pdxscholar@pdx.edu.

Authors

Jennifer S. Gorce, Mark J. Caddick, Ethan F. Baxter, Besim Dragovic, John C. Schumacher, Robert J. Bodnar, and Jamie F. Kendall

Geochemistry, Geophysics, Geosystems

RESEARCH ARTICLE

10.1029/2021GC009716

Special Section:

Insights into Subduction Zone Processes from Models and Observations of Exhumed Terranes

Key Points:

- Metamorphic garnets record two stages of growth during HP/LT metamorphism and exhumation of the Cycladic Blueschist Unit (CBU) on Syros, Greece
- Garnet growth spanned 4.8 ± 2.1 Myr including decompression from 2.1 to 1.6 GPa
- Garnets in this sample record a part of the CBU that was exhumed as a series of tectonic slices on Syros

Supporting Information:

Supporting Information may be found in the online version of this article.

Correspondence to:

J. S. Gorce,
jgorce@lpi.usra.edu



Citation:

Gorce, J. S., Caddick, M. J., Baxter, E. F., Dragovic, B., Schumacher, J. C., Bodnar, R. J., & Kendall, J. F. (2021). Insight into the early exhumation of the Cycladic Blueschist Unit, Syros, Greece: Combined application of zoned garnet geochronology, thermodynamic modeling, and quartz elastic barometry. *Geochemistry, Geophysics, Geosystems*, 22, e2021GC009716. <https://doi.org/10.1029/2021GC009716>

Received 11 FEB 2021

Accepted 15 JUL 2021

Insight Into the Early Exhumation of the Cycladic Blueschist Unit, Syros, Greece: Combined Application of Zoned Garnet Geochronology, Thermodynamic Modeling, and Quartz Elastic Barometry

Jennifer S. Gorce^{1,2,3} , Mark J. Caddick¹ , Ethan F. Baxter⁴, Besim Dragovic⁵, John C. Schumacher⁶, Robert J. Bodnar¹, and Jamie F. Kendall⁴

¹Virginia Tech, Blacksburg, VA, USA, ²Lunar and Planetary Institute, USRA, Houston, TX, USA, ³Astromaterials Research and Exploration Sciences, NASA JSC, Houston, TX, USA, ⁴Boston College, Boston, MA, USA, ⁵University of South Carolina, Columbia, SC, USA, ⁶Portland State University, Portland, OR, USA

Abstract Constraining conditions and mechanisms of the early stages of exhumation from within subduction zones is challenging. Although pressure, temperature, and age can be inferred from the exhumed rock record, it is generally difficult to derive each of these parameters from any single rock, thus demanding assumptions that diverse data from multiple samples can be safely combined into a single pressure-temperature-time (P - T - t) path that might then be used to infer tectonic context and mechanisms of exhumation. Here, we present new thermobarometric and geochronologic information preserved in a single sample from Syros, Greece, to deduce the conditions and rates of the earliest phase of exhumation as a part of the well-preserved high-pressure metamorphic rocks of the Cycladic Blueschist Unit (CBU). The sample studied here is a garnet-bearing, quartz-mica schist that records two distinct metamorphic events. Results from thermodynamic models and quartz-in-garnet elastic geobarometry show that metamorphic garnet cores formed as P - T conditions evolved from $\sim 485^\circ\text{C}$ and 2.2 GPa to 530°C and 2.0 GPa, and that garnet rims formed as conditions evolved from $\sim 560^\circ\text{C}$ and 2.1 GPa to $\sim 550^\circ\text{C}$ and 1.6 GPa. Sm-Nd geochronology on garnet cores and rims yields ages of 45.3 ± 1.0 and 40.5 ± 1.9 Ma, respectively, thus indicating a 4.8 ± 2.1 Myr growth span. Given the decompression path calculated based on garnet core and rim P - T estimates, we conclude that the distinct phases of garnet growth preserve evidence of the initial exhumation of portions of the CBU.

Plain Language Summary Constraining the evolution of rocks formed at great depths (>60 km) and their subsequent return to Earth's surface is a challenging endeavor, because information regarding the pressure, temperature, and timing of formation is typically elucidated through the study of multiple samples and thus through the comparison of different datasets. Here, we present pressure, temperature, and age data that were derived by analyzing garnet crystals within a single sample from a well-known paleo-subduction zone located in Syros, Greece. Our results show that the sample records two metamorphic events that occurred as a result of initial ascent to the surface from depths of ~ 66 to 48 km.

1. Introduction

The island of Syros, Greece is known for its well-preserved paleo-subduction zone lithologies of the Cycladic Blueschist Unit (CBU), including high-pressure metamorphic rocks that have been interpreted to represent the slab/mantle interface at depths of >60 km (e.g., Breeding et al., 2004; Bröcker & Enders, 2001; Dixon et al., 1987). Understanding the evolution of high-pressure rocks, such as these lends insight into metamorphic processes including dehydration and densification of the oceanic lithosphere, and hydration and melting of the lithospheric mantle (e.g., Caron and Pequignot, 1986; Duesterhoeft et al., 2014; Hacker et al., 2003; Peacock, 1993, 2004; Ridley, 1984). It is important to constrain the conditions and durations over which these processes occur, as they greatly influence global volatile budgets and heat transfer, convergent margin seismicity, felsic crustal genesis, and the formation of explosive eruptive volcanoes (e.g., Bebout, 1991, 1995; Hacker et al., 2003). The prograde evolution of exhumed subduction zone rocks is becoming increasingly well understood (e.g., Behr et al., 2018; Kotowski & Behr, 2019; Laurent et al., 2018; Philippon et al., 2011), as are the timescales and the depth range over which cooling following (near)

isothermal decompression occurs (e.g., Ring et al., 2020; Skelton et al., 2019). However, the mechanisms of detachment from the subducting slab and rates at which initial exhumation proceeds are still poorly understood. Accordingly, here we develop a pressure-temperature-time (P - T - t) path that constrains the rate of exhumation of the CBU during the first ~25 km of ascent.

The mechanisms associated with exhumation, and particularly the onset of exhumation, are debated, and a variety of tools have been employed in order to better understand the ways that subducted lithologies are returned to the surface. Many exhumation models have invoked channel flow mechanics, where either up-dip sediment flow forces the return of HP lithologies (Cloos, 1982) or serpentinization of ultramafic lithologies along the slab/mantle interface forms a weak, low-density channel where flow can be induced (e.g., Gerya et al., 2002; Hermann et al., 2000). This ultimately allows blocks of metabasic material to be transported upward. Previous studies have suggested that the size and location of these blocks influences the exhumation path of eclogitic material and that juxtaposition of blocks containing metamorphic assemblages with different P - T - t histories is possible (Cloos, 1982; Federico et al., 2007; Neilsen & Marschall, 2017). Field evidence for this process has been documented in the form of “*mélange terrains*” in which eclogitic blocks within a serpentinitic (or chloritic) matrix are interpreted to represent zones of intense physical and chemical mixing along the slab/mantle interface (e.g., Bebout, 2007; Bebout & Barton, 2002; Cloos & Shreve, 1988; Marschall & Schumacher, 2012; Penniston-Dorland et al., 2010; Spandler et al., 2008).

Numerical simulations that characterize channel flow using parameters, such as convergence rate, degree of hydration, rheologic properties, temperature, and duration of the process have provided insights into the evolution of channel flow. These studies have shown that a minimum serpentine channel thickness is required to produce density contrasts between peridotite and serpentinite sufficiently large to drive ascent (Schwartz et al., 2001). Ultimately, forced channel flow can contribute to the development of a low viscosity zone along the slab/mantle interface (e.g., Herbert et al., 2009) and aid the buoyancy forces driving exhumation (e.g., Gerya et al., 2002). Such flow is predicted to result in multiple episodes of burial and exhumation, in which a given block can move vertically multiple times before its final exhumation to the surface. In some cases, metamorphic mineral assemblages may be preserved as a complex and perhaps cryptic P - T - t paths that could have either clockwise or counter clockwise components (e.g., Gerya et al., 2002).

Recent studies of high-pressure rocks in the Aegean (e.g., Laurent et al., 2016; Roche et al., 2016) use a combination of geochronological and structural constraints to suggest that synorogenic deformation caused localized zones of extension, particularly along shear bands, resulting in exhumation. In some cases, rollback of the subducting slab is cited as an additional driving force, where moderate upward flow in the subduction channel (Brun & Faccenna, 2008; Husson et al., 2009) combines with localized regions of extensional faulting to bring deeply (>60 km) subducted material to the surface. It has been suggested that the onset of slab rollback in the Hellenides (e.g., Schellart, 2004; Royden & Husson, 2006) initiated decoupling of the CBU at ~50 Ma, with blueschist metamorphism of the CBU at ~45 Ma during synorogenic exhumation (e.g., Laurent et al., 2018; Lister & Forster, 2016; Roche et al., 2016), highlighting the fact that multiple exhumation mechanisms likely operate in tandem in order to exhume subducted lithologies. This is particularly important to consider on Syros, because the upper unit of the CBU, well exposed in N. Syros, exhibits *mélange* characteristics while the lower unit of the CBU, well exposed in S. Syros, contains more cohesive volcano-sedimentary sequences (Keiter et al., 2011), suggesting that different exhumation mechanisms are in operation.

The pressure-temperature-time (P - T - t) paths experienced by exhumed metamorphic rocks can place important constraints on subduction zone processes. Path geometry and calculated heating, burial, and exhumation rates can be coupled with field observations and structural data to infer tectonic mechanisms (e.g., Maruyama et al., 1996). In recent years, techniques for determining the P - T - t histories of metamorphic rocks have become increasingly sophisticated and include a wide range of chemical, isotopic and elastic mineral barometers, thermometers, and chronometers. These have contributed to a growing set of important studies of the high-pressure terranes exposed in the Cycladic islands (e.g., Ashley et al., 2014; Brocker et al., 1993; Keiter et al., 2004; Laurent et al., 2016; Philippon et al., 2013; Trotet, Jolivet, & Vidal, 2001; Trotet, Vidal & Jolivet, 2001). While many of these studies constrain the thermal, barometric, or temporal evolution of subducted lithologies of the Aegean plate, combined interpretations commonly require assumptions regarding

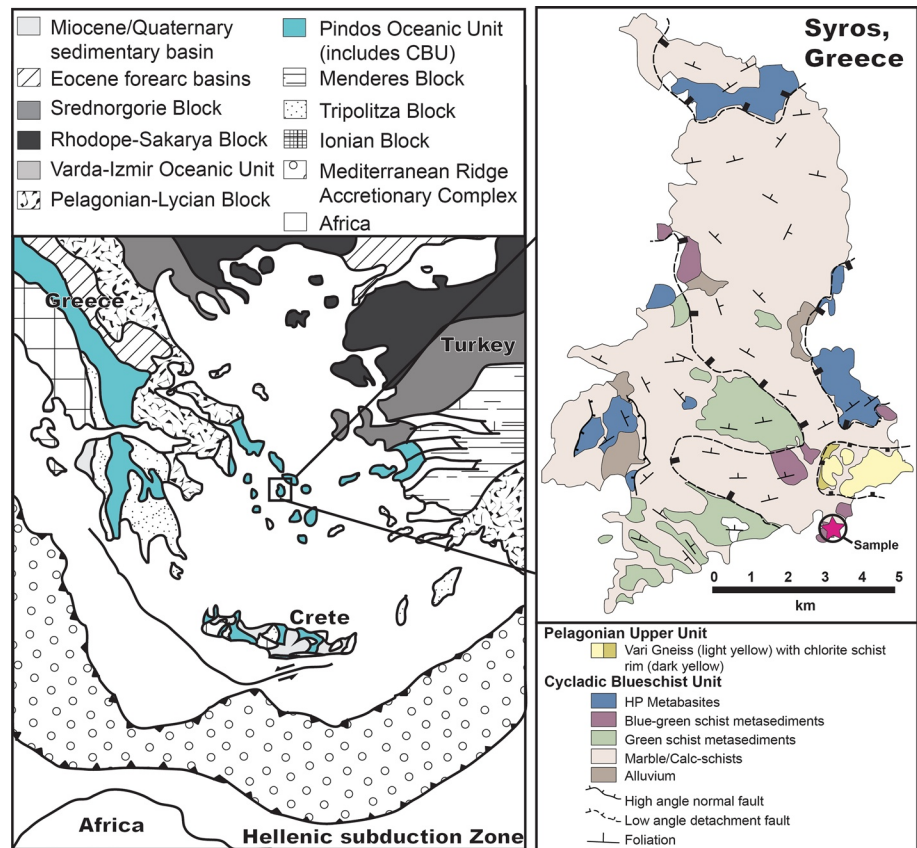


Figure 1. Left: Simplified geologic map of the Aegean region, modified after Ring et al. (2010). The extent of the Pindos Oceanic unit, which includes the Cycladic Blueschist Unit, is shaded in blue and Syros, Greece is located in the black box. Right: Simplified geologic map of Syros (modified after Behr et al., 2018; Keiter et al., 2004), with the location sample 14HSY-35E indicated by the pink star (GPS: 37°23'08.0" and 024°56'53.7").

the relationships among multiple samples, while examples giving ranges of pressure, temperature, and age within the same sample are rare.

Here, we present new temperature, pressure, and age data preserved in zoned metamorphic garnets from a single sample from Syros, Greece and discuss likely exhumation mechanisms for the CBU. We use thermodynamic modeling to estimate the P - T conditions of two garnet growth events, testing and affirming assumptions of thermodynamic equilibration by utilizing quartz-in-garnet elastic geobarometry as an independent barometer. The P - T results are coupled with high precision Sm-Nd garnet geochronology on garnet core and rim portions to establish the duration of garnet growth.

2. Geological Setting

The modern Hellenic subduction zone is located in the Aegean Sea south of Crete, and represents the continued subduction of the Adriatic and later African plate beneath the Aegean plate that started in the Mesozoic (Figure 1). The resulting orogenic belt, the Hellenides, is comprised of several distinctive tectonic subunits that were progressively subducted from 145 to 50 Ma (Krohe & Mposkos, 2002; Lips et al., 1998; Mposkos & Kostopoulos, 2001; Ring & Layer, 2003; Sherlock et al., 1999; von Quadt et al., 2005). Most studies agree that at least three oceanic domains, the Vardar-Izmir Oceanic Unit, the Pindos Oceanic Unit, and the East Mediterranean Ocean, were subducted over the course of ~80 Myr.

In this study, we examine a sample from the Pindos Oceanic Unit, which is a heterogeneous domain of continental and oceanic lithologies. While Tremblay et al. (2015) demonstrated that there is not much evidence for oceanic crust in the Pindos domain, we use the term in the colloquialism of studies such as Ring and

Layer (2003). The upper and lower parts of the Pindos Oceanic unit include the Selcuk Mélange and the CBU, respectively (Okrusch & Broecker, 1990). The CBU is interpreted to be the most deeply exhumed segment of the Hellenides, which records widespread eclogite-facies conditions that are typically attributed to equilibration at 60 km depth or more. The CBU is comprised of graphite-bearing schists and orthogneisses as well as graphite-bearing marbles, metapelites, and metavolcanics (Durr et al., 1978; Ring et al., 2010; Ring & Layer, 2003). Well-preserved remnants of the CBU are found on the island of Syros, Greece (Figure 1).

On Syros, the CBU is represented by a series of stacked tectonic nappes, with higher metamorphic grade rocks thrust onto lower grade material (Trotet, Vidal, & Jolivet, 2001). The CBU is subdivided into two major units: (a) volcanoclastic material separated by the Kastri basal fault (Philippon et al., 2011; Schumacher et al., 2008) and (b) the Kampos oceanic series, which crops out as a *mélange* sequence in which metabasic and metavolcanic units are surrounded by a matrix of serpentinite. Previous studies have speculated that the Kampos series represents the slab-mantle interface (e.g., Breeding et al., 2004), though recent geochemical evidence suggests that the serpentinites form in a hyper-extended margin setting instead (Cooperdock et al., 2018; Gyomlai et al., 2021). Lithologies from the Syros Kampos unit have long been the focus of subduction zone studies because both eclogite-blueschist metamorphism and variable greenschist overprinting (e.g., Ridley, 1984) are well preserved. The Vari Unit is tectonically juxtaposed to the CBU in the southeast portion of the island. Most studies concluded that it represents the hanging wall of a low angle detachment (e.g., Keiter et al., 2004; Laurent et al., 2016; Soukis & Stockli, 2013), although Philippon et al. (2011) suggested that the Vari unit represents basement material that was thrust on to younger lithologies. Almost all observed lithologies on Syros are strongly deformed (e.g., Keiter et al., 2011; Rosenbaum et al., 2002; Schumacher et al., 2008) and show metamorphic foliation and penetrative linear fabric. The timing of deformation with respect to metamorphism has been the subject of many structural studies and interpretations include syn-metamorphic (e.g., Rosenbaum et al., 2002; Trotet, Vidal, & Jolivet, 2001) and post-metamorphic deformation (e.g., Keiter et al., 2004).

3. Timing and Metamorphism of the CBU on Syros

Evidence for blueschist and eclogite-grade metamorphism on Syros can be found in exceptionally well-preserved high-pressure minerals, such as aragonite (Brady et al., 2004), lawsonite (Keiter et al., 2004), and glaucophane (Dixon et al., 1987; Schumacher et al., 2008). Although most well-preserved, high-pressure lithologies are reported from the northern Kampos unit on Syros, high-pressure mineral assemblages can be found throughout the island (Behr et al., 2018; Kotowski & Behr, 2019; Laurent et al., 2016; Schumacher et al., 2008; Skelton et al., 2019; this study).

Ages for the Pindos Unit protolith range from Triassic to Eocene (e.g., Jones & Robertson, 1991; Okrusch & Broecker, 1990; Ring et al., 2010; Ring & Layer, 2003), with an age for a gabbroic protolith constrained by U-Pb zircon geochronology at 80–75 Ma (Keay, 1998) and by Lu-Hf zircon geochronology at 80 ± 12.4 –13.8 Ma (Tomaschek et al., 2003). Peak metamorphism is generally thought to have occurred between 53 and 40 Ma. The older ages in this spectrum are constrained by Lu-Hf garnet ages in eclogites (Lagos et al., 2007) and U-Pb ages of zircons found as an inclusion in garnet that grew during prograde to peak metamorphism (Tomaschek et al., 2003), and are typically reported in samples collected from the *mélange* terrains predominately located in N. Syros. The younger ages in this spectrum are typically recorded in the lower, more cohesive volcano-sedimentary units found in S. Syros (Cliff et al., 2017; Laurent et al., 2016) and are constrained by the dating of white micas with the K-Ar, Ar-Ar, and Rb-Sr systems (Brocker et al., 2013; Lagos et al., 2007 and references herein; Maluski et al., 1987), though some studies report white mica ages as old as 53 Ma (e.g., Tomaschek et al., 2003).

Some of the recent geochronological studies have sought to derive a tectonic context for the CBU lithologies on Syros by focusing on white mica age populations. For example, Cliff et al. (2017) analyzed a suite of phengitic (K-rich white mica) samples from primarily blueschist-facies lithologies on Syros and, using Rb-Sr dating techniques, reported ages of 53–46 Ma for the most northern HP/LT metamorphic belt (top of structural pile), and ages of 42–30 Ma in the southern portions of Syros. They combined these results with extensional fabrics and concluded that blueschist-facies overprinting associated with extensional faulting must have taken place from 42 to 30 Ma. Similarly, conclusions were drawn by Lister and Forster (2016)

using an asymptotes and limits approach to Ar-Ar data (Forster & Lister, 2004). Other studies concluded that populations of white-mica age data represent different periods of blueschist- and greenschist-facies overprinting, and range in age from ~45 to 20 Ma (Forster & Lister, 2005; Uunk et al., 2018). Skelton et al. (2019), who reported ages of 38–43 Ma for units located in S. Syros near Fabrika, concluded that the CBU is a subduction-related nappe stack that is comprised of at least three metamorphic belts. The spread in mica ages is typically interpreted to reflect a combination of cooling through the closure temperatures of these systems, excess Ar, and/or the presence of multiple generations of mica, all of which have been invoked to question whether mica ages preserve peak metamorphism, or some other process (Lagos et al., 2007; Laurent et al., 2018; Putlitz et al., 2005). Similarly metamorphic ages of ~50 Ma are reported for the nearby island of Sifnos, based on high precision Sm-Nd garnet geochronology (Dragovic et al., 2015), and the metamorphic histories of Sifnos and Syros are frequently compared (e.g., Laurent et al., 2018; Schumacher et al., 2008; Tomaschek et al., 2003; Trotet, Jolivet, & Vidal, 2001; Trotet, Vidal, & Jolivet, 2001).

Using a variety of geothermobarometers, previous studies have reported a range of pressures (1.7–2.2 GPa) and temperatures (500°C–550°C) for peak metamorphism of the CBU (e.g., Ashley et al., 2014; Dixon, 1976; Dragovic et al., 2012; Keiter et al., 2004; Lister & Raouzaïos, 1996; Philippon et al., 2013; Ring et al., 2010; Schumacher et al., 2008; Trotet, Vidal, & Jolivet, 2001). For example, Dixon (1976) placed lower limits of peak metamorphism at 1.4 GPa and 450°C–500°C based on assemblages of jadeite + quartz and zoisite + paragonite + quartz + lawsonite and the absence of lawsonite + jadeite. Ridley (1984) placed upper limits at 2.0 GPa and 575°C based on paragonite stability. More recently, studies have constrained *P* and *T* of rocks from Syros and Sifnos using the coexistence of glaucophane + aragonite (Schumacher et al., 2008), multi-equilibria thermobarometry using TWEEQ (Berman, 1991; Trotet, Vidal, & Jolivet, 2001), and thermodynamic modeling of mineral assemblages and compositions (e.g., Dragovic et al., 2012, 2015). In addition to dating peak metamorphism on Sifnos, Dragovic et al. (2012, 2015) constrained the rate of garnet growth, implying heating rates of $22.3 \pm 8.0^\circ\text{C}/\text{Myr}$ over the integrated growth history of garnet, and $>75^\circ\text{C}/\text{Myr}$ in the final stages of prograde metamorphism.

Additionally, substantial research has focused on constraining overprinting greenschist metamorphism in the CBU. On Syros, parts of the CBU are overprinted with greenschist mineral assemblages that can either be associated with variable extents of rehydration of subducted material during near-isothermal decompression (Bröcker et al., 2013; Brooks et al., 2019; Marschall et al., 2006; Trotet, Vidal, & Jolivet, 2001), or related to deformation during exhumation (e.g., Keiter et al., 2004; Ring & Layer, 2003; Soukis & Stöckli, 2013). Temperatures and pressures for greenschist overprinting are estimated to be between 350°C–450°C and 0.6–1.3 GPa, as determined by the stability of mineral assemblages including chlorite, epidote, glaucophane, and lawsonite pseudomorphs (Breeding et al., 2004; Laurent et al., 2018; Marschall et al., 2006; Matthews & Schliestedt, 1984; Skelton et al., 2019; Trotet, Vidal, & Jolivet, 2001). An additional pulse of retrograde metamorphism has been dated at 25–21 Ma (Bröcker et al., 2013) and a final sub-greenschist overprinting event occurred around 12–8 Ma (Ring & Layer, 2003; Soukis & Stöckli, 2013).

While many studies have rigorously constrained portions of the *P-T-t* path of the CBU, the rates and conditions of the early stages of exhumation of the CBU remain poorly understood. Here, we focus on elucidating the timing and conditions of the final phases of prograde blueschist- and eclogite-facies metamorphism, and the rate and *P-T* path during the early stages of exhumation. This information provides important constraints on the timescales and processes associated with the detachment and initial exhumation phase that preceded the previously constrained greenschist-facies overprinting conditions.

4. Sample Description

Sample 14HSY-35E is a garnet-bearing quartz-mica schist which also contains amphibole, clinopyroxene, carbonate, epidote, and titanite (Figure 2). Micro-inclusions of omphacitic clinopyroxene are found in quartz (Figure 2b), which is itself commonly included in or intergrown with glaucophane. These textural relationships suggest that the HP-LT metamorphic mineral assemblage in the observed thin section contained garnet, quartz, clinopyroxene, phengite, and rutile. Phengite and finely intermixed quartz bands define the primary foliation (Figure 2c). Glaucophane needles and paragonite are sub-parallel to each other

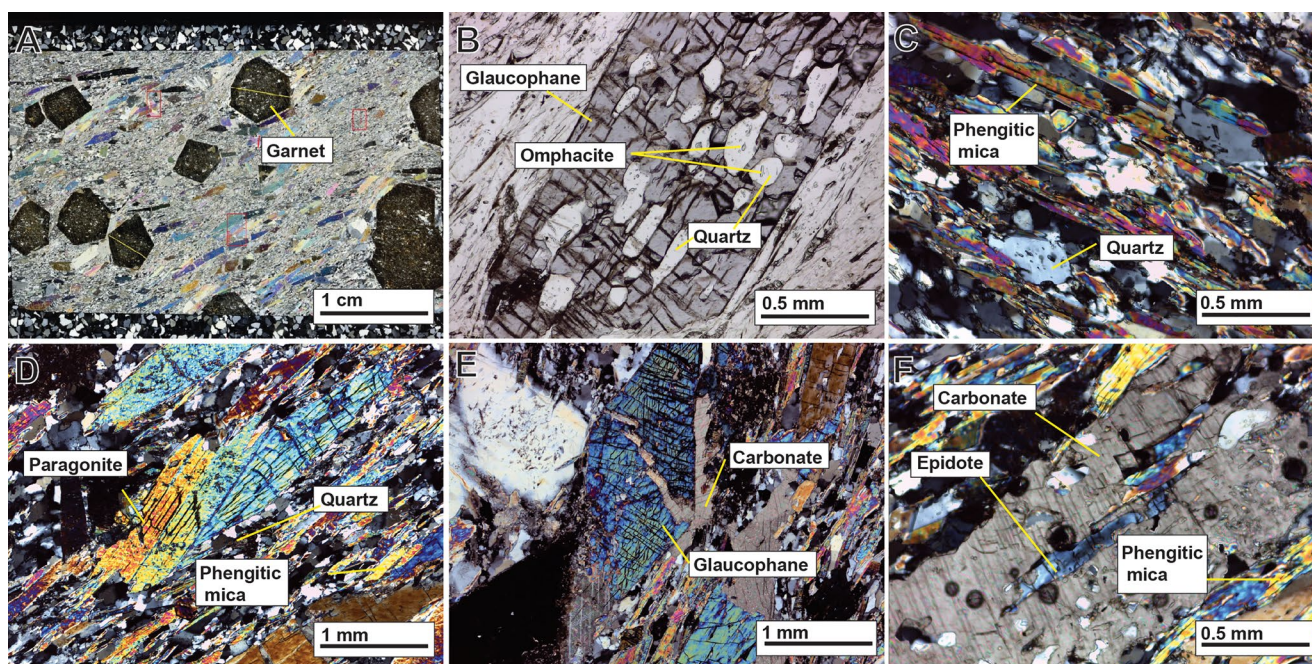


Figure 2. Photomicrographs of sample 14HSY-35E. (a) Thin section image in cross-polarized light. (b) Omphacite inclusions in quartz, which is overgrown by later glaucophane. (c) Phengitic mica defining the primary foliation. (d) Paragonite overgrowing quartz and phengitic mica. (e) Late carbonate phase overgrowing glaucophane. (f) Late carbonate phase overgrowing epidote.

and oriented in the primary foliation plane, but clearly overgrow phengite and quartz (Figures 2b and 2d). Calcite overgrows glaucophane and epidote (Figures 2e and 2f).

Porphyroblastic garnets are abundant and all contain inclusion-rich cores and inclusion-poor rims (Figure 2a). Core inclusion assemblages consists of quartz, rutile, clinopyroxene, and epidote. Garnet crystal rims contain sparse, small ($\sim 10\text{--}15\ \mu\text{m}$) quartz, epidote, and apatite inclusions. On average, the garnet rims are $\sim 500\ \mu\text{m}$ thick and noticeably paler orange in color compared to the garnet cores. The paler, inclusion poor rims correspond with elevated concentrations of Mn (Figure 3). Overall, garnet crystals are relatively homogeneous in size ($\sim 4\text{--}7\ \text{mm}$ diameter).

5. Methodology

5.1. Chemical Analyses

A representative portion of the sample was crushed and major-element chemistry was determined via X-ray fluorescence (XRF) at Franklin and Marshall College, with maximum $\text{Fe}^{3+}/\text{Fe}^{2+}$ determined via titration (Table 1). An alternate bulk rock composition was determined from point-counted mineral abundances and average mineral compositions determined via electron microprobe analysis (EMPA). This composition was used to assess possible hand-specimen-scale compositional heterogeneities and to provide a more accurate composition for the specific area of the petrographic observations.

Minerals were analyzed at Virginia Tech using a Cameca SX-50 electron microprobe with a 20 nA beam current and 15 kV accelerating voltage. Representative compositions of pyroxene, quartz, mica, amphibole, epidote, and titanite are shown in Table 2. Wavelength dispersive spectrometry maps and spot analysis traverses through garnet porphyroblasts were collected to reveal major element zoning (Figure 3).

5.2. Phase Equilibrium Calculations

We constructed isochemical phase diagrams based on the compositions determined by XRF and point count analyses, calculating thermodynamically stable mineral assemblages and their compositions over a range

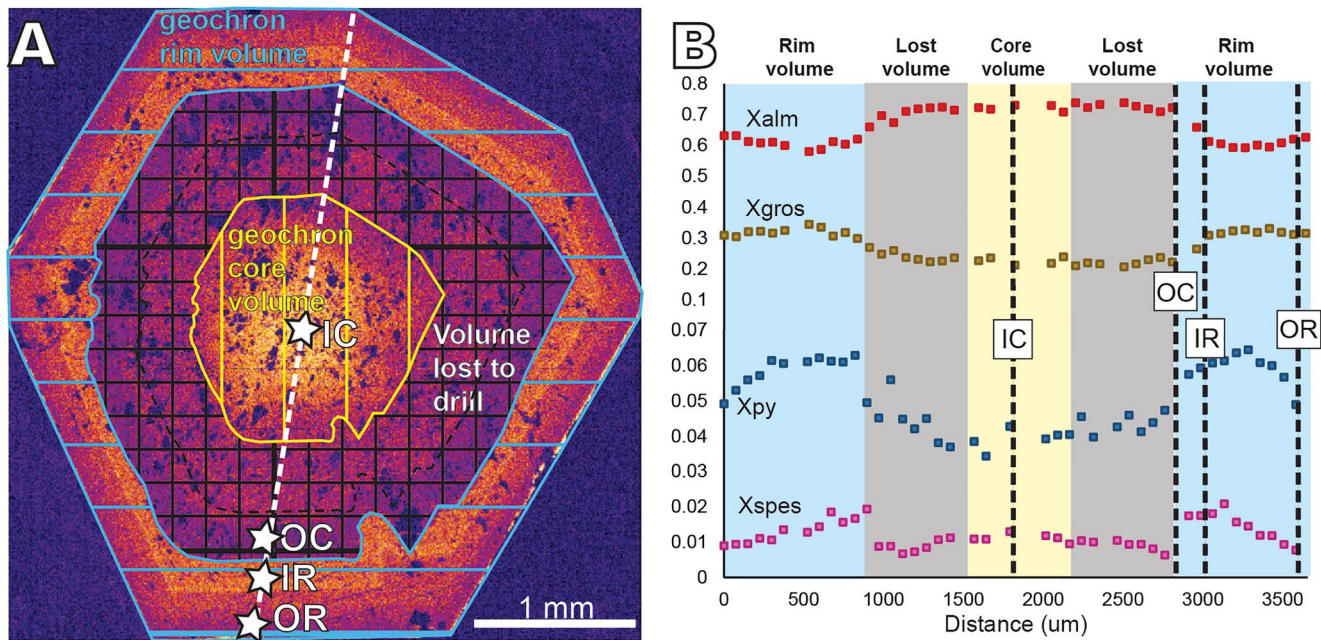


Figure 3. Left: Qualitative Mn map collected via WDS mapping of a garnet porphyroblast in sample 14HSY-35E. The area shaded in yellow represents the volume of garnet sampled for “core” age geochronology. The area shaded in blue represents the volume of garnet used for “rim” age analyses. The area shaded in black represents the volume of garnet lost during the micro-drilling process (~800 μm trench). The points labeled as IC, OC, IR, and OR (inner core, outer core, inner rim, outer rim, respectively), are locations and compositions along a quantitative electron microprobe analysis (EMPA) transect (white dashed line) used for calculating P - T evolution during garnet growth. Right: Quantitative EMPA analyses of garnet, expressed as a mole fraction of end-members. Points that fall within the yellow region correlate with garnet core compositions, points that fall within the blue regions correlate with garnet rim composition, and points that fall within the shaded gray region would have been lost in the micro-drill trench. Black dashed lines labeled as IC, OR, IR, and OR correlated to labeled white stars in the left image.

of P - T conditions (Figure 4). Calculations in the chemical system K_2O - MnO - MgO - CaO - Al_2O_3 - FeO - Fe_2O_3 - SiO_2 - Na_2O - TiO_2 utilized the program *Perple_X* (Connolly, 2005) and the ds5.5 (2004) update of the Holland and Powell (1998) thermodynamic data set. Solution models for complex phases are listed in Table 3. Saturation of a H_2O - CO_2 fluid was assumed ($X_{\text{H}_2\text{O}} = 0.999$), and the Compensated Redlich-Kwong model of Holland and Powell (1991) was used. A more thorough discussion on fluids during metamorphism can be found in Section 7.3.

5.3. Fractionating the Bulk Rock Composition

Refractory phases, such as garnet can fractionate elements from the system as they grow, which modifies the residual reactive bulk rock composition as the system continues to evolve (i.e., Marmo et al., 2002; Tracy

Table 1
Bulk Compositional Data Used in Thermodynamic Models

| Reactive composition | SiO_2 | TiO_2 | Al_2O_3 | MgO | CaO | MnO | FeO | Fe_2O_3 | Na_2O | K_2O |
|----------------------|----------------|----------------|-------------------------|--------------|--------------|--------------|--------------|-------------------------|-----------------------|----------------------|
| XRF | 64.25 | 0.68 | 15.38 | 2.48 | 4.97 | 0.15 | 6.77 | 1.06 | 1.82 | 2.43 |
| Point count | 64.89 | 1.15 | 15.60 | 2.68 | 4.12 | 0.08 | 6.14 | 0.68 | 2.38 | 2.28 |
| -50 vol % gt | 66.08 | 0.73 | 14.97 | 2.56 | 4.58 | 0.12 | 5.30 | 1.13 | 1.94 | 2.60 |
| -52 vol % gt | 66.11 | 0.73 | 14.96 | 2.56 | 4.57 | 0.12 | 5.28 | 1.13 | 1.94 | 2.60 |
| -99 vol % gt | 68.03 | 0.77 | 14.53 | 2.64 | 4.16 | 0.09 | 3.74 | 1.20 | 2.07 | 2.77 |

Note. The reactive bulk rock composition labeled as “point count” was used to confirm that the XRF analysis was representative of the observed mineral assemblage in thin section.

XRF, X-ray fluorescence.

Table 2
Characteristic Mineral Compositions for Major and Minor Phases Present in Sample 14HSY-35E Measured via EMPA

| | Pyroxene | Amphibole | K-mica | Na-mica | Epidote | Titanite |
|--------------------------------|----------|-----------|--------|---------|---------|----------|
| SiO ₂ | 58.63 | 58.51 | 54.78 | 49.65 | 40.10 | 31.95 |
| TiO ₂ | 0.03 | 0.01 | 0.24 | 0.07 | 0.11 | 34.86 |
| Al ₂ O ₃ | 12.06 | 12.08 | 27.21 | 41.46 | 28.61 | 2.64 |
| MgO | 6.01 | 8.50 | 3.68 | 0.13 | 0.00 | 0.00 |
| CaO | 11.46 | 0.66 | 0.01 | 0.15 | 24.14 | 30.30 |
| MnO | 0.03 | 0.03 | 0.00 | 0.01 | 0.03 | 0.02 |
| FeO | 7.17 | 12.98 | 3.00 | 0.29 | 6.99 | 0.20 |
| Na ₂ O | 7.64 | 7.20 | 0.38 | 7.52 | 0.02 | 0.02 |
| K ₂ O | 0.01 | 0.02 | 10.71 | 0.72 | 0.00 | 0.00 |

Note. Analyses for garnet compositions are presented in Table 4.

et al., 1976). To account for this, we progressively modified the bulk rock composition to simulate increasing garnet abundance and component sequestration in garnet. Mass was “subtracted out” from the bulk rock composition based on the composition of garnet determined via EMPA (Figure 3) and the abundance of garnet in the sample. Four critical points were identified in the zoning profiles (the compositions of two garnet crystals at these points are given in Table 4):

1. Inner Core (IC) = the geometric and chemical core (center) of crystals, assumed to represent the beginning of garnet growth if crystals grew uniformly in all directions and are sectioned through the core in the third dimension.
2. Outer Core (OC) = the edge of the inclusion-rich zone (coinciding with a minimum in the Mn concentration along traverses), assumed to represent the end of the first growth episode (50% of garnet growth)
3. Inner Rim (IR) = the beginning of the inclusion-free rim (coinciding with a stepwise increase in Mn content), assumed to represent the re-initiation of garnet growth (52% of garnet growth)
4. Outer Rim (OR) = the outer edge of the garnet crystal, assumed to represent the end of garnet growth (99% of garnet growth)

Bulk rock compositions were calculated for each of these domains (Table 2), with isochemical phase diagrams calculated for each (Figure 4).

5.4. Sm-Nd Garnet Geochronology

Garnets were plucked whole from a rough crush (0.5–1 cm), cut adjacently to the material used in XRF analyses of the bulk rock, and were selected based on size (only crystals >4 mm in diameter were used to avoid geochronology results that would be bias toward rim ages). Crystals were mounted on carbon blocks and cut with a diamond micro-saw to produce 2-mm-thick garnet wafers. Distinct cores and rims could be identified with the naked eye, as the rim is noticeably paler in color than the core. On this basis, 21 wafered garnet crystals were micro-drilled to separate core and rim domains using methods described in Pollington and Baxter (2011). Garnet cores and rims from all 21 samples were lumped together to have enough material for bulk core and bulk rim Sm-Nd isotopic analysis. Note that we did not attempt to differentiate between the inner/outer cores or inner/outer rims observed in the microprobe image (Figure 3), due to the small size of the crystals (4–7 mm diameter) compared to sample lost in the micro-drill trench (~800 μm width). Thus, the resolution of our *P-T* constraints, which includes calculated *P-T* conditions for the inner core, outer core, inner rim, and outer rim separately (see Section 6.1), is finer than that of the age resolution, which is limited to a bulk core (inner plus outer) and bulk rim (inner plus outer) age. Microdrill trenches were placed such that only outer core material would be lost to the drilling (Figure 3) so our core age is dominated by the inner core. Garnet cores and rims, bulk rock samples, and samples of the matrix (without garnet) were crushed and sieved (100–200 mesh). Crushed garnet was passed through a Frantz magnetic separator and manually hand-picked in an initial attempt to remove all phases that were not garnet.

Once crushed to a grain size of 75–100 μm, inclusion phases in garnet were removed using partial dissolution techniques from Starr et al. (2020). Several fine powders were also treated in order to preferentially remove inclusion phases. All samples, including treated and untreated garnet crushes and powders, as well as rock powders, were fully dissolved. Sm and Nd isotopic ratios were analyzed on an Isotopx Phoenix thermal ionization mass spectrometer at the Center for Isotope Geochemistry at Boston College following the methods of Harvey and Baxter (2009). Nd isotopes were loaded with 2 μL of 2N nitric acid onto Re filaments with 2 μL of tantalum oxide (Ta₂O₅) activator slurry added to facilitate greater sample ionization. Samples were run in multi-dynamic mode as the oxide species (NdO⁺). Sm was loaded with 2 μL of 2N nitric onto Ta filaments and run in static mode as metal species (Sm⁺). Instrumental mass fractionation was normalized to ¹⁴⁶Nd/¹⁴⁴Nd = 0.7219 and to ¹⁴⁹Sm/¹⁵²Sm = 0.516860 using an exponential mass fractionation correction. Over the period of this study, repeat analysis of an in-house 4 ng Ames Nd standard yielded 0.5121530 ± 0.0000085 ppm 2σ (*n* = 11) and ¹⁴⁷Sm/¹⁴⁴Nd external reproducibility is 0.054%, based on repeat

analysis of a gravimetrically calibrated mixed Sm-Nd solution. In isochron error propagation, the larger (poorer) of the external precision reported above or the internal analytical precision (in Table 5) was used (Baxter et al., 2017). Finally, three-column blanks run alongside samples ranged from 3 to 16 pg of Nd, and were thus deemed negligible.

5.5. Quartz in Garnet Geobarometry

We used elastic barometry of quartz inclusions in garnet to determine the entrapment pressure of quartz where it was overgrown by garnet, in order to test and verify assumptions made during phase equilibria modeling. Because Raman peak positions of α -quartz vary with pressure and temperature (Schmidt & Ziemann, 2000), and host minerals, such as garnet are sufficiently rigid to maintain high inclusion pressures following exhumation (Enami et al., 2007), numerous studies have used peak positions of Raman bands to determine residual inclusion pressures of quartz in garnet. Then, the entrapment pressure can be estimated using appropriate equation of state (EoS; e.g., Angel et al., 2014; Ashley et al., 2014; Kohn, 2014; Kouketsu et al., 2014; Spear et al., 2014).

To determine the residual inclusion pressure on quartz inclusions in garnet, we measured quartz Raman spectra with a JY Horiba LabRam HR800 spectrometer at the Department of Geosciences at Virginia Tech. Spectra were collected using a 514.57 nm argon laser with a 800 mm focal length spectrometer (1,800 lines/mm grating). Thirty-two quartz inclusions from two garnet crystals in one thick section (60 μm thick) were analyzed (16 analyses per garnet), using a confocal microscope with a 400 μm hole, 150 μm slit, and 100X objective lens. Analyses were collected over a 30 s accumulation time with three iterations. A spectral range of 100–800 cm^{-1} was used in order to measure the 464, 206, and 128 cm^{-1} quartz peaks. Three argon plasma lines (520.30, 266.29, and 116.04 cm^{-1}) and a Herkimer diamond standard were measured for calibration purposes. Raman lines were fitted with Peakfit v4.12 using the Pearson IV model that allows variable peak asymmetry, following procedures described by Schmidt and Ziemann (2000). The Pearson IV model is similar to the Voigt Gaussian/Lorentz area model used by Cisneros et al. (2020) to fit peaks of quartz inclusions in epidote. A summary of these data can be found in the supporting information. Quartz inclusions were selected based on size (10–20 μm), their relationship with fractures, thick section surfaces and other inclusions, and their distribution throughout the host garnet. We determine residual inclusion pressures using the hydrostatic experiments from Schmidt and Ziemann (2000) and then used Ashley et al. (2014) and Kohn (2014) fits to data. Typical inferred pressure precision was between ± 0.11 and 0.15 kbars; determined by propagating the error of the peak positions of standards ($\pm 0.1 \text{ cm}^{-1}$ in the reproducibility of the 464 cm^{-1} quartz standard peak), peak positions of unknowns, and instrument uncertainty.

Entrapment pressures were calculated with the software package EosFit-Pinc (Angel et al., 2017), an add-on for the EosFit7 software package (Angel et al., 2014). The EoS for almandine was from Milani et al. (2015) and the EoS for quartz is from Angel et al. (2017), and includes elastic softening in both alpha and beta quartz and a curved alpha-beta phase boundary. We used the composition of garnet adjacent to inclusions in order to constrain temperatures needed for determining entrapment pressures. We assumed that temperature increased linearly from 485°C to 530°C during the first stage of garnet growth (inner core to outer core) and that temperature decreased linearly from 560°C to 550°C during the second stage of garnet growth (inner rim to outer rim). A summary of quartz and garnet thermodynamic and elastic properties use can be found in the supporting information.

The success of inclusion-host barometry relies on the assumption that the host phase behaves rigidly, and that both inclusion and host phase relax elastically during decompression. To behave as a rigid body, the host must have a high shear modulus and act as an infinite medium (Ashley et al., 2014; Enami et al., 2007; Kohn, 2014; Zhang, 1998; Zhong et al., 2020). Though garnet has a high shear modulus, the assumption that it acts as an infinite medium does not always hold true (Zhang, 1998), especially where garnet crystals contain a large number of relatively closely spaced inclusions (as is the case with the garnet cores examined here). To account for this assumption, we carefully examined the garnet surrounding each inclusion (within an area 3X the radius of the inclusion radius; e.g., Zhang, 1998; Zhong et al., 2020) at 40X and 100X optical magnification, excluding all inclusions for which this region contained less than 20% nongarnet phases (i.e., other inclusions).

6. Results

6.1. *P-T* Modeling

Electron microprobe analyses reveal a distinct change in garnet composition that coincides with the boundary between the inclusion-rich cores and inclusion-free rims described in Section 4 (Figure 3). This boundary separates two discrete garnet growth events, and we apply thermodynamic models to constrain the *P-T* conditions associated with these two growth episodes.

Garnet compositions suggest that the mineral assemblage associated with initial growth included glaucophane + dolomite + lawsonite + omphacite + quartz + white mica + rutile, and occurred at $\sim 485^\circ\text{C}$ and 2.2 GPa (inner core, Figure 4a, $\pm 50^\circ\text{C}$ and ± 0.15 GPa, as shown in the figure and applicable to all thermodynamic pressures and temperatures described below. Uncertainties taken from Palin et al. (2016)). This is consistent with the observed inclusion assemblage, other than the presence of epidote inclusions, which we

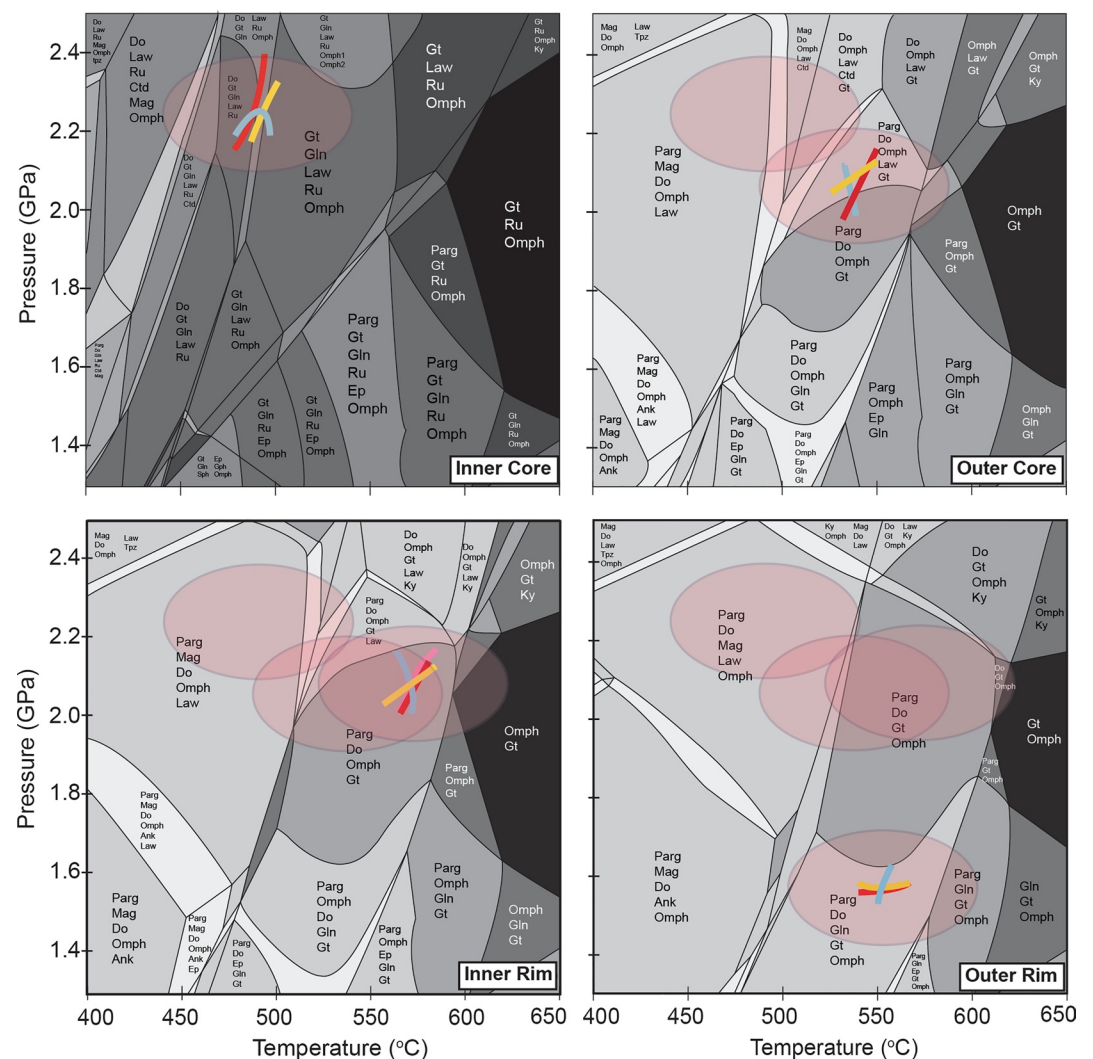


Figure 4. Isochemical phase diagrams constructed to estimate equilibration pressures and temperatures for different stages of garnet growth: Inner core (IC), outer core (OC), inner rim (IR), and outer rim (OR), respectively. The bulk rock X-ray fluorescence composition was input to represent the reactive bulk rock composition at the beginning of garnet growth. For each progressive model, the volumetric contribution of pre-existing garnet was subtracted from the reactive bulk rock composition (see Table 1 for values). Isopleth colors represent concentrations of X_{Mn} (pink) X_{Fe} (red), X_{Ca} (yellow), and X_{Mg} (blue) measured in garnet. Error ellipses (red) span $\pm 50^\circ\text{C}$ and ± 0.15 GPa, as determined from Palin et al. (2016) and are superimposed onto the succeeding panel.

Table 3
Solution Models Used for End-Member Mixing in Thermodynamic Models

| Mineral | Solution model | Source |
|------------|----------------------|---|
| Cpx | Omph (GHP2) | Green et al. (2007) and Diener and Powell (2012) |
| Opx | Opx (HP) | Holland and Powell (1998) |
| Epidote | Ep (HP) | Holland and Powell (1998) |
| Garnet | Gt (WPPH) | White et al. (2005) |
| Feldspar | Feldspar | Fuhrman and Lindsey (1988) |
| Chlorite | Chl (HP) | Holland and Powell (1998) |
| Chloritoid | Ctd (HP) | Holland and Powell (1998) |
| Titanite | Sp (WPC) | White et al. (2002) |
| Amphibole | cAmph (DP2) | Deiner et al. (2007) and Deiner et al. (2008) |
| Ilmenite | IlGkPy | |
| Mica | Mica (CHA) | Coggon and Holland (2002) and Auzanneau et al. (2009) |
| Biotite | Bio (HP) | Holland and Powell (1998) |
| Carbonate | M (HP) and oCcM (HP) | Holland and Powell (1998) |

suggest resulted from lawsonite breakdown during decompression and therefore do not represent primary inclusion phases. Garnet is inferred to have continued to grow during decompression and heating, and the outer core grew at $\sim 530^\circ\text{C}$ and ~ 2.0 GPa (outer core, Figure 4b).

Calculated phase equilibria for a bulk composition corrected for the removal of mass during formation of garnet crystal cores (i.e., the zone between the inner core and outer core in Figure 3) suggest that the inner part of the garnet rim (IR in Figure 3) grew at ~ 2.1 GPa and 560°C (Inner rim, Figure 4c), in the presence of paragonite, dolomite, omphacite, rutile, and quartz. Garnet crystal rims contain too few inclusions to confirm this assemblage, with thermodynamic models discussed in detail below (Figure 5) showing the modal abundance of glaucophane reduced from approximate 20 vol% during garnet core growth to 15 vol% during outer rim growth and the modal abundance of lawsonite reduced to zero over the same interval.

Results presented in Figure 4 is based on the bulk-rock composition of sample 14HSY-35E, from which we manually calculated modified bulk compositions to simulate sequestration of elements by garnet, using garnet abundances estimated from thin section observations (Table 2). In an alternative approach, we calculated phase equilibria at 1°C increments along a P - T path derived by joining the equilibration conditions determined for the garnet inner core, outer core, inner rim, and outer rim (i.e., the four panels of Figure 4). In this case, the bulk rock composition of sample 14HSY-35E served as an initial input, with progressive modification of this composition after each P - T increment at which garnet and/or fluid was calculated to be stable. The mineralogy that is predicted to form as the system evolves is shown in Figure 5. Results are consistent with garnet core formation between 485°C , 2.2 GPa and 530°C , 2.0 GPa. A second phase of growth to produce the garnet rims occurs between 560°C , 2.1 GPa and 550°C , 1.6 GPa. Results also confirm that garnet was likely stable below 485°C and 2.2 GPa, implying that overstepping of the garnet-forming reaction may have played a role in the first stage of garnet growth, as previously inferred for other CBU lithologies (Castro & Spear, 2017; Dragovic et al., 2012). For most minerals, model results and observed abundances agree within 1–2 wt% after the growth of the outer garnet rim (Table 6). The two main discrepancies between predictions and observations, that is, the over-estimation of epidote and mica abundances and underestimation of dolomite abundance by the model, are explored in greater detail in the discussion. Given the good agreement between calculated mineral evolution and thin section observations, we suggest that equilibrium was maintained during most of the inferred history of formation of 14HSY-35E. This interpretation is examined further below with inclusion-host barometry.

Table 4
Characteristic of Major 2+ Cation Concentrations in Garnet Along With Critical Points Described in Text and Illustrated in Figure 3

| | Garnet 1 | | | | Garnet 2 | | | |
|----|-----------------|-----------------|-----------------|-----------------|-----------------|-----------------|-----------------|-----------------|
| | X_{Fe} | X_{Mn} | X_{Mg} | X_{Ca} | X_{Fe} | X_{Mn} | X_{Mg} | X_{Ca} |
| C1 | 0.731 | 0.013 | 0.043 | 0.213 | 0.733 | 0.029 | 0.028 | 0.210 |
| R1 | 0.710 | 0.008 | 0.044 | 0.238 | 0.710 | 0.007 | 0.046 | 0.237 |
| C2 | 0.660 | 0.018 | 0.058 | 0.265 | 0.651 | 0.018 | 0.048 | 0.283 |
| R2 | 0.621 | 0.009 | 0.057 | 0.313 | 0.637 | 0.007 | 0.050 | 0.306 |

Table 5
Isotopic Analyses From Garnet Core and Rim Populations, Determined via TIMS

| | Samples | Sm147/ Nd144 | SE (2σ) | Nd143/Nd144 | SE (2σ) | Sm (ppm) | Nd (ppm) | Nd (ng) |
|-------------|--------------|-----------------|----------|-------------|-----------|-------------|----------|------------|
| Garnet core | Aliquot 1 | 0.41749 | 0.00015 | 0.5126363 | 0.0000094 | 1.352 | 1.958 | 18 |
| | Aliquot 2 | 0.72333 | 0.00018 | 0.512735 | 0.000012 | 0.914 | 0.764 | 4.0 |
| | Dirty powder | 0.14748 | 0.00057 | 0.5125682 | 0.0000058 | 2.568 | 10.33 | 92 |
| | Powder 1 | 1.7753 | 0.0080 | 0.513036 | 0.000028 | 0.741 | 0.252 | 3.7 |
| | Powder 2 | 1.9403 | 0.0088 | 0.513093 | 0.000014 | 0.733 | 0.228 | 5.4 |
| | Powder 3 | 2.01378 | 0.00033 | 0.513122 | 0.000026 | 0.646 | 0.194 | 3.9 |
| Garnet rim | Aliquot 1 | 0.046405 | 0.000038 | 0.5125412 | 0.0000084 | 0.526 | 6.854 | 29 |
| | Aliquot 2 | 0.87164 | 0.00010 | 0.5127552 | 0.0000076 | 0.292 | 0.202 | 6.1 |
| | Dirty powder | 0.6322 | 0.0027 | 0.512708 | 0.000041 | 0.297 | 0.284 | 4.2 |
| | Powder | 0.12095 | 0.000023 | 0.512551 | 0.000027 | 1.632 | 8.160 | 17 |
| Bulk | Whole rock | 0.104468 | 0.000012 | 0.5125457 | 0.0000063 | 1.972 | 11.42 | 14 |
| | Matrix | 0.101574 | 0.000017 | 0.5125469 | 0.0000061 | 2.835 | 16.89 | 22 |

Note. All garnet samples were cleaned using methods described in Starr et al. (2020) unless indicated (labeled “dirty”). “Aliquots” represent garnet crushed to 75–100 μm grain sizes and “powders” are fine (<75 μm grain size) garnet residues collected during the crushing process.

6.2. Quartz in Garnet Geobarometry

Calculated entrapment pressures of analyzed quartz inclusions in two selected garnet crystals (Figure 6) are in the range 0.7–2.1 GPa, with most analyses falling between 1.7 and 1.9 GPa. Due to the high inclusion density in the garnet cores, some of the analyzed inclusions did not meet the 2–3X radial distance criteria and may be overpressured. However, results are generally within uncertainty of pressures calculated by thermodynamic models, as indicated by the overlapping fields associated with geologic uncertainty in thermodynamic modeling (± 0.15 GPa, Palin et al., 2016), and with the uncertainty associated with geobarometry (± 0.2 GPa, Bonazzi et al., 2019; ~ 0.1 – 0.2 GPa, Thomas & Spear, 2018). We recognize that one could arguably fit either an isobaric or decompression pressure profile through the quartz inclusion barometry data (Figure 6). However, similar metamorphic pressures to those determined via thermodynamic modeling were calculated for samples from Fabrika (3 km from our sample site) by Skelton et al. (2019), and

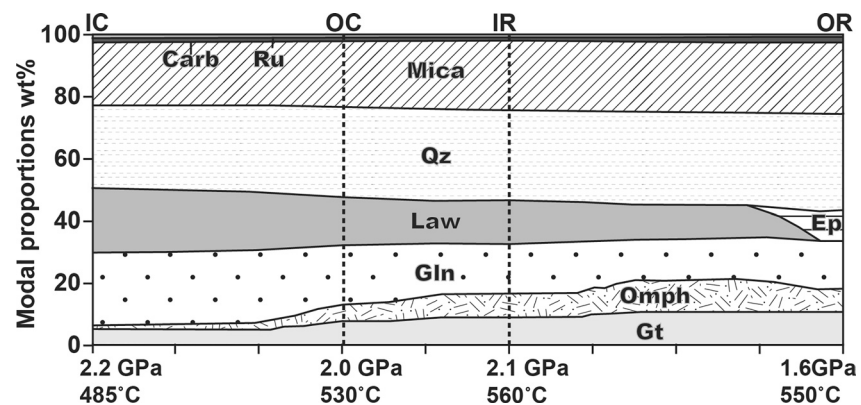


Figure 5. Calculated mineralogic evolution of a rock having the composition of sample 14HSY-35E along the P - T path representing complete formation of garnet from inner core to outer rim. The beginning of the path is the P - T formation condition of the inner core (IC), with the P - T conditions of outer core (OC), inner rim (IR), and the outer rim (OR) also shown. The stable mineral assemblage and abundances were calculated assuming that the XRF-determined bulk rock composition is appropriate for the inner core, with both garnet and aqueous fluid then removed at each successive P - T condition if they were stable (i.e., present) at the previous condition.

Table 6
Mineral Modal Abundances (Vol%) Determined for 14HSY-35E

| Mineral | Model | Point count |
|-------------|-------|-------------|
| White mica | 23.4 | 27.6 |
| Dolomite | 1.5 | 4.8 |
| Garnet | 11 | 12 |
| Glaucophane | 15.6 | 14.3 |
| Omphacite | 7.5 | 7.3 |
| Lawsonite | 0 | 0 |
| Quartz | 31 | 27.7 |
| Rutile | 0.7 | 0 |
| Epidote | 9.3 | 3.2 |
| Titanite | 0 | 3 |

Note. Calculated mineral abundancies (model) were determined from Figure 5 at 1.6 GPa and 550°C.

the reproducibility of calculated pressures of garnet growth suggest that inferences of crystal growth during decompression is justified.

The general overlap between results from thermodynamic modeling and those from quartz-in-garnet geobarometry provides confidence that these results reasonably describe the pressure evolution during garnet formation. However, several quartz inclusions preserve entrapment pressures that are significantly lower than suggested by both thermodynamic models and the majority of quartz inclusion barometry (by up to ~0.5 GPa; Figure 6). Most notably, one inner core quartz inclusion in each garnet crystal (points A and C in Figure 6), one inner rim inclusion from Garnet 1 (point B in Figure 6), and one outer core inclusion in Garnet 2 (point D in Figure 6), preserve lower pressures, outside the uncertainty bounds of the thermodynamic models.

Several possibilities may explain the outliers shown on Figure 6. Some of the quartz inclusions may be close to unrecognized cracks within the garnet host, resulting in lower confining pressures on the inclusions. This is especially applicable to inclusions located relatively close to the surface of the thick section. Proximity can also have an effect on the inclusion

pressure. Accordingly, high magnification photomicrographs of the four “outlier inclusions” and four of the “consistent” inclusions are presented in Figure 7. In each case, the outlier inclusions appear to be in contact with or in close proximity to other quartz inclusions. In comparison, the high-pressure inclusions are more

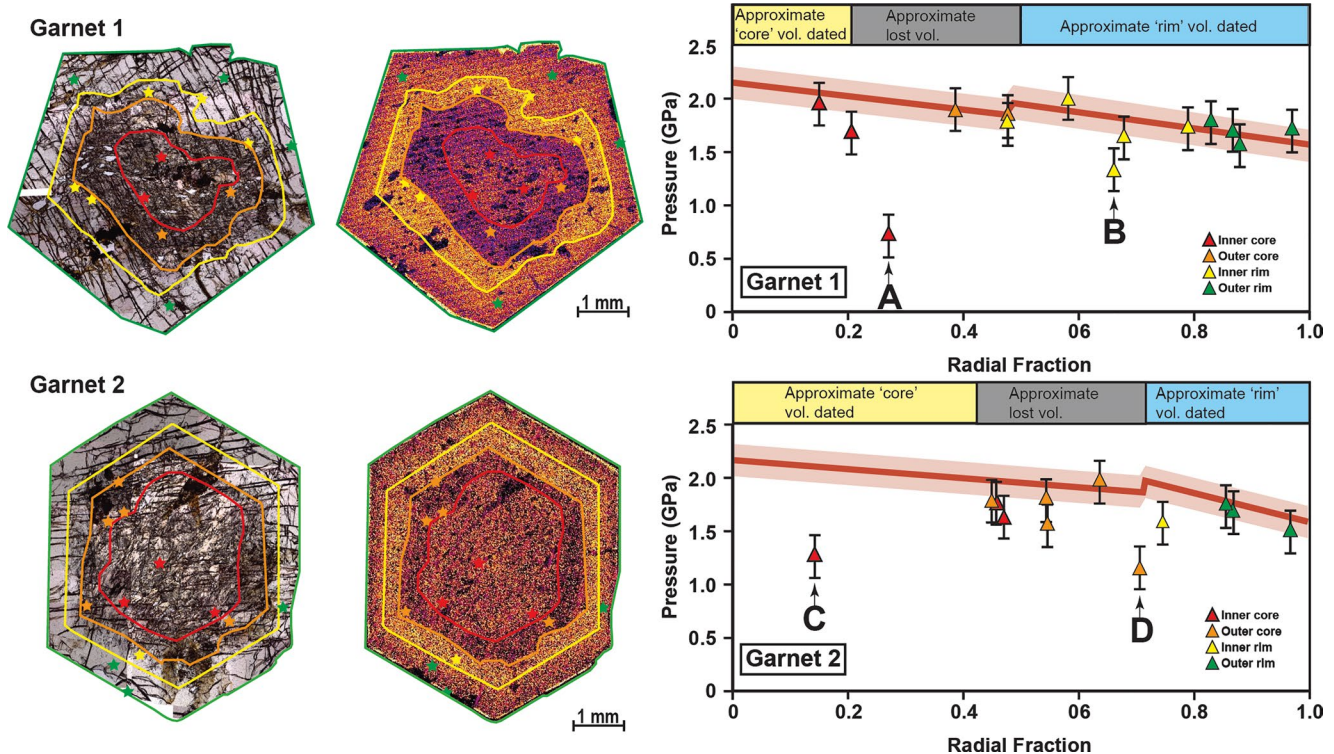


Figure 6. Entrapment pressures determined by quartz-in-garnet geobarometry for inclusions in two garnet porphyroblasts. Triangles in right and left panels represent calculated trapping pressures, color coded according to the chemical zones identified in the garnet images to the left, and plotted as a distance from the garnet core (center of crystal). The points labeled as (A–D) corresponds to a photomicrograph contained in Figure 7 demonstrating the spatial relationship of the inclusions. Uncertainty in inclusion entrapment pressures (± 0.2 GPa) after Bonazzi et al. (2019). The dark red line is the pressure profile calculated for garnet growth in Figure 4, with a ± 1.5 GPa uncertainty envelop (light red) based on results from Palin et al. (2016). The yellow box represents the approximate volume of garnet sampled for “core” age and the blue box represents the volume of garnet used for “rim” age. The gray box represents the volume of garnet lost during the micro-drilling process.

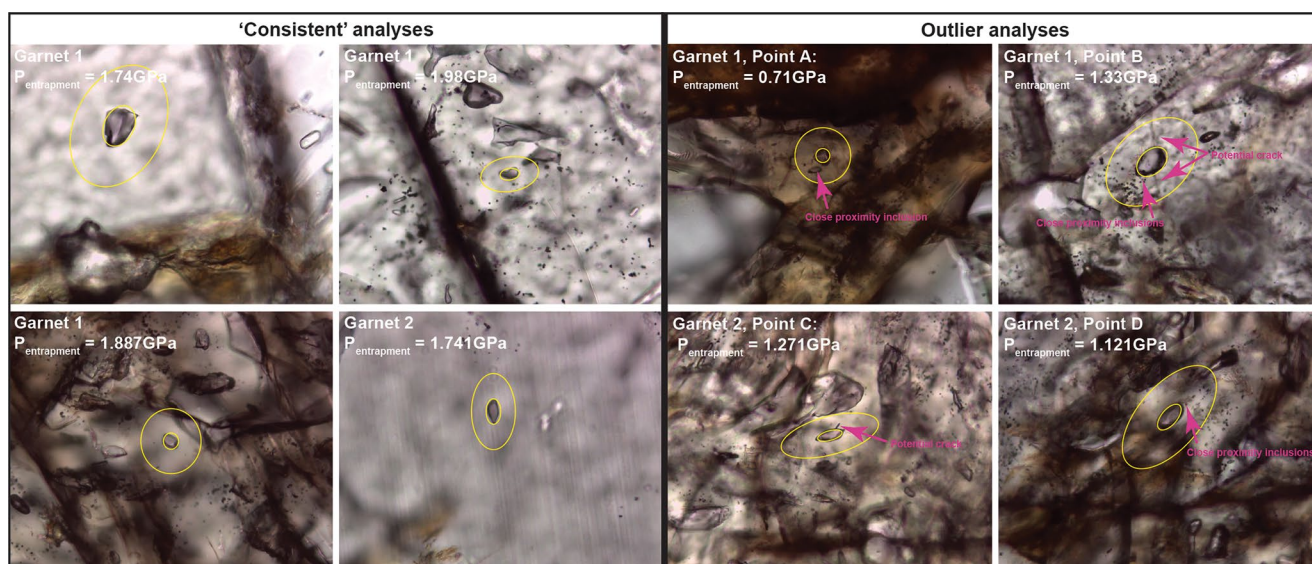


Figure 7. Outlier analyses: High magnification (40X) photomicrographs of the four “outlier analyses” from inclusion barometry results. These data met the filtration criteria (less than 20% nongarnet phases within 3-radii of the inclusion of interest), but yielded entrapment pressures that were lower than the majority of inclusion measurements. Each panel corresponds to a data point indicated in Figures 6a–6d. Consistent analyses: High magnification photomicrographs (40X) of four “consistent analyses” from inclusion barometry results. These data met the filtration criteria and yielded entrapment pressures that are representative of the majority of inclusion measurements and consistent with thermodynamic modeling results.

isolated within the garnet host. A final possibility is that the geometry of the quartz inclusion itself affects the pressure recorded by the inclusion. This phenomenon has been experimentally observed by Bonazzi et al. (2019), who demonstrated that an anisotropic inclusion shape yields entrapment pressures that vary up to 1.4 GPa from known experimental conditions. On this basis, we consider the low pressures returned from these four outlier inclusions to not be representative of the P - T conditions of formation of the host garnet, and they are not considered further. After excluding these data, Raman pressures and thermodynamic modeling yield consistent results.

6.3. Sm-Nd Garnet Geochronology

Ages calculated for garnet cores and rims are 45.3 ± 1.0 Ma (2σ ; MSWD = 1.02, $n = 7$) and 40.5 ± 1.9 Ma (2σ ; MSWD = 0.99, $n = 5$), respectively (Figure 8). A summary of isotopic values and associated uncertainties can be found in Table 5. The magnitude and precision of Nd concentration, $^{147}\text{Sm}/^{144}\text{Nd}$ ratio, and $^{143}\text{Nd}/^{144}\text{Nd}$ ratio is influenced by the extent to which REE-bearing inclusion phases were removed from the garnets during partial dissolution, as well as sample size and subsequent signal intensity during TIMS analysis.

The 7-point isochron (Figure 8) generated for the garnet core population includes $^{147}\text{Sm}/^{144}\text{Nd}$ and $^{143}\text{Nd}/^{144}\text{Nd}$ values from the whole rock, several garnet core separates, and several garnet core fine powders. The whole-rock is included in the garnet core isochron because at the time of initial garnet growth, garnet crystals would be in isotopic equilibrium with the bulk rock, due to the fact that significant garnet growth has yet to fractionate the reactive bulk rock composition (Baxter et al., 2017). A 5-point isochron generated for the garnet rim population consists of $^{147}\text{Sm}/^{144}\text{Nd}$ and $^{143}\text{Nd}/^{144}\text{Nd}$ values from the bulk rock matrix (representing the reactive bulk rock composition at the time of rim growth), garnet rim separates, and garnet rim fine powders. Given the MSWD near 1.0 for both the core and rim ages, there is no evidence for heterogeneous garnet ages amongst the 21 garnet crystals lumped together for core and rim analysis outside reported age uncertainty. These ages represent the timing of garnet core and rim growth throughout this hand sample.

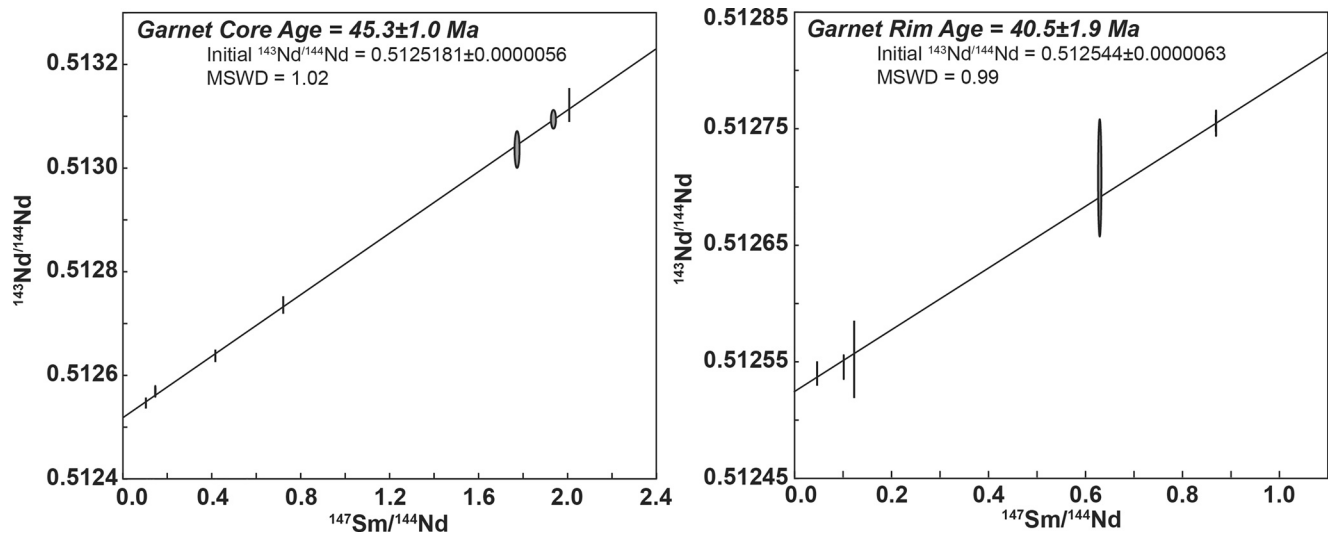


Figure 8. Isochron for garnet core growth: 45.3 ± 1.0 Ma (MSWD = 1.02, $n = 7$) and garnet rim formation: 40.5 ± 1.9 Ma (MSWD = 0.99, $n = 5$). All reported uncertainties are 2σ .

7. Discussion

7.1. Did Garnet Grow Under Equilibrium Conditions?

Several studies (e.g., Spear, 2017; Spear et al., 2014; Wolfe & Spear, 2018) report that phase equilibria modeling may not be an appropriate method to determine P - T conditions of metamorphism due to sporadic or persistent failures of rocks to achieve or maintain equilibrium. Evidence for such departures from equilibrium is indeed observed in the compositional zoning of garnet (Carlson et al., 2015) and is also inferred in other cases (e.g., Dragovic et al., 2012; Hoschek, 2013; Wolfe & Spear, 2018) in which garnet is predicted to have initially grown at P - T conditions well above the garnet isograd. If initial garnet growth substantially overstepped the equilibrium garnet-in conditions, alternate methods may be required to estimate the initial garnet composition (Spear, 2017). Many studies have argued that such overstepping is necessary for crystal growth because the reaction affinity (macroscopic driving force of a reaction) for garnet nucleation is relatively high and thus requires a significant activation energy to overcome kinetic barriers (Carlson et al., 2015; Spear & Patterson, 2017).

Given this, it might be argued that quartz-in-garnet barometry results presented here provides evidence for a single phase of isostatic (i.e., both isothermal and isobaric) garnet growth, commonly interpreted as reflecting rapid growth as soon as the system overcomes the energy barrier to nucleation. Several recent studies have extended this to conclude that zoned garnet crystals that were initially interpreted to represent progressive growth during burial and heating instead grew at isobaric and isothermal conditions following substantial overstepping of the garnet isograd (Spear & Wolfe, 2019). However, given the garnet zoning in the sample studied here, the sharp transition in inclusion abundance at the garnet core-rim boundaries, and importantly, the 4.8 ± 2.1 Myr timescale of garnet growth determined here, we rule this interpretation out in this case. We acknowledge that substantial overstepping prior to initial garnet growth is possible, but nucleation impediments are not an issue during the rim overgrowths on a preexisting garnet substrate. That, coupled with the statistically different ages of the texturally and compositionally different garnet domains implies that a single brief episode of garnet growth following overstepping is unlikely. It is quite possible, however, that the core itself did grow over a short duration. Results presented here (Figure 6) show that thermodynamic modeling of the growth conditions of garnet are within error of the results from elastic barometry. While this may not be a general case (e.g., Wolfe & Spear, 2018), it is clear that thermodynamic modeling captures the growth conditions of the garnet in this study.

7.2. Comparing P - T - t Results With Previous Studies

Results from thermodynamic models (Figure 4) indicate that garnet in 14HSY-35E grew in two stages during decompression, with one stage from 2.2 GPa and 485°C to 2.0 GPa and 530°C (inner core-outer core) and the other from 2.1 GPa and 560°C to 1.6 GPa and 550°C (inner rim-outer rim). However, it should be noted that the uncertainty ellipses in Figure 4 (± 0.15 GPa and $\pm 50^\circ\text{C}$, as determined based on the uncertainties reported in Palin et al., 2016) suggest that potential pressure fluctuations in the first three stages of garnet growth (inner core, outer core, and inner rim) are not resolvable within the reported uncertainties. Thus, no additional tectonic conclusions can be inferred based on their relative change, and models suggesting small amplitude pressure variations cannot be tested further with this dataset (e.g., Beltrando et al., 2007; Lister & Forster, 2016; Rubatto et al., 2011; Viete et al., 2018). However, the P - T conditions of the final stage of garnet growth (outer rim) are outside the uncertainty of the first three estimates, implying that inferences of garnet growth during or after some degree of decompression are justified. These results are in general agreement with maximum pressure (1.7–2.0 GPa) and temperature (500°C–550°C) ranges determined for the CBU by previous studies (e.g., Ashley et al., 2014; Dixon, 1976; Dragovic et al., 2012; Keiter et al., 2004; Lister & Raouzaos, 1996; Philippon et al., 2013; Ring et al., 2010; Schumacher et al., 2008; Trotet, Vidal, & Jolivet, 2001). Furthermore, the two stages of metamorphic garnet growth predicted here agree with the recent findings of Skelton et al. (2019), who used garnet core compositions, co-existing inclusion stability, and lawsonite stability to estimate that at least two stages of metamorphism, that occurred at pressures of ~ 1.2 – 1.9 and ~ 2.1 – 1.3 GPa, respectively, are preserved on parts of S. Syros. Given that lawsonite is retained in some Syros rocks and kyanite is always absent, we note that high-temperature decompression further into lawsonite-absent fields is unlikely. Our inferred P - T path just exceeds the maximum limit of lawsonite stability (e.g., Hamelin et al., 2018; Schumacher et al., 2008), implying either differential high- T exhumation of various lithologies on the island (i.e., some lithologies exceeded this limit but many did not), or sluggish kinetics of lawsonite breakdown in some cases.

Sm-Nd ages of garnet cores and rims (45.3 ± 1.0 and 40.5 ± 1.9 Ma, respectively), are consistent with the younger ages reported for blueschist/eclogite metamorphism of the CBU in general (~ 42 – 46 Ma). We interpret the younger garnet rim age to reflect outer rim growth during or after some degree of decompression because (a) by volume the average age is dominated by the outer rim and (b) most garnets are zoned such that Sm concentrations are constant or increasing toward the rim (e.g., Kohn, 2009; Gatewood et al., 2015). It is interesting to note that the garnet rim age determined in this study (40.5 ± 1.9 Ma) is in good agreement with the mica Rb/Sr ages reported from the same area (Fabrika, Figure 1) by Skelton et al. (2019; 38–43 Ma) whereas the garnet core age reported in our study is older (45.3 ± 1.0 Ma). This is not surprising as the Sm-Nd garnet age of the core preserves an earlier part of the prograde P - T - t path compared to the garnet rim and Rb-Sr in mica ages reported in Skelton et al. (2019). The garnet core age thus records the maximum metamorphic pressures preserved in 14-HSY-35E while mica ages and garnet rims record maximum metamorphic temperatures preserved in 14-HSY-35E as depicted in Figure 9. Other published garnet geochronology from Syros comes from Lagos et al. (2007) and samples further north on the island; these Lu-Hf garnet ages are significantly older, 50–52 Ma. This garnet growth age difference may reflect tectonic or bulk compositional differences between the dated samples or differences in Lu versus Sm zonation where bulk Lu-Hf ages may bias toward the early onset of growth compared to Sm-Nd ages (e.g., Baxter et al., 2017; Kohn, 2009).

7.3. Were Fluids Present During Metamorphism?

Textures observed in thin section can be used to infer the role of fluids during the metamorphism of 14HSY-35E. For example, textural relationships between garnet crystals and their inclusions imply that the HP-LT mineral assemblage contained garnet, quartz, clinopyroxene, phengite and rutile, and epidote. This mineral assemblage is also predicted by thermodynamic models (Figures 4 and 5) with the exception of the observation of epidote. We interpret that epidote inclusions found in garnet formed through lawsonite breakdown, which is consistent with previous observations of epidote \pm white mica pseudomorphs after lawsonite in other high pressure lithologies on Syros (e.g., Hamelin et al., 2018). This suggests that the breakdown of lawsonite was likely the primary driver for dehydration during garnet growth in 14HSY-35E. Thermodynamic modeling results, extracted from Figure 5, suggest that ~ 2 wt% H_2O was lost from the bulk rock

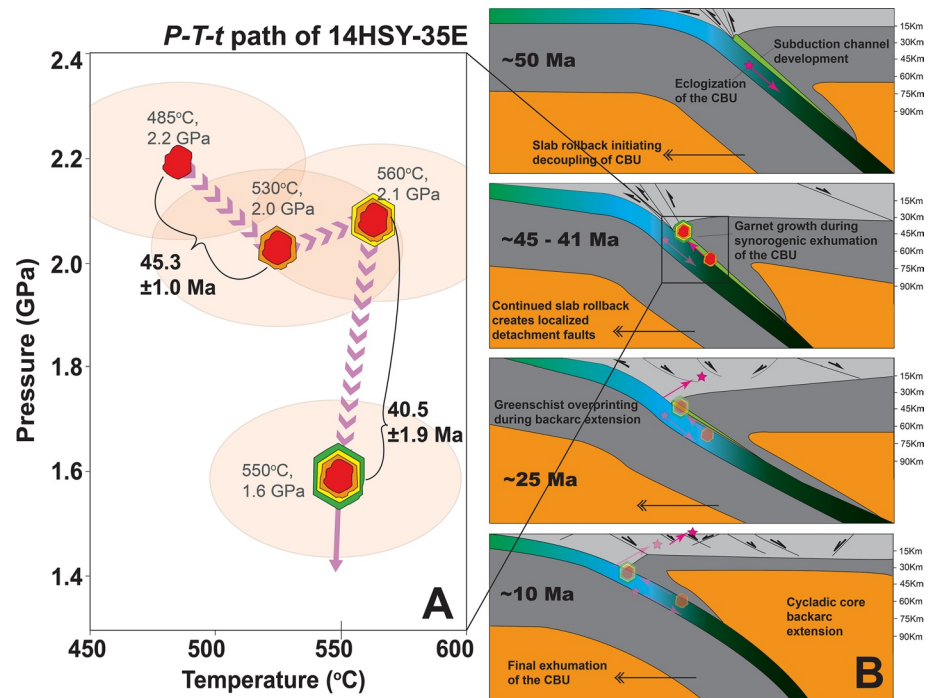


Figure 9. (a) Calculated P - T - t path for sample 14HSY-35E. (b) Potential geologic setting for sample 14HSY-35E, modified from Roche et al. (2016).

composition along the calculated P - T path. Calculations suggest that lawsonite represented 20 wt% of the modal mineralogy at the beginning of garnet growth, with complete absence of lawsonite and the stability of epidote by the end of garnet grown (Figure 5).

Other mineral relationships imply that sample 14HSY-35E interacted with aqueous fluids after HP-LT metamorphism. For example, the primary foliation in the matrix of 14HSY-35E has been overgrown by late-stage glaucophane needles and paragonite (Figures 2b and 2d), suggesting that hydrous fluids were available during retrogression. This interpretation is further supported by the presence of fluid inclusions in recrystallized quartz. These fluid inclusions likely formed from fluids produced by breakdown of high-pressure hydrous phases, and these same liberated fluids were incorporated into greenschist-facies minerals (Brooks et al., 2019). Studies of B isotopes in metasomatic tourmaline further suggest that fluids in Syros underwent significant alteration during interactions with surrounding material during exhumation or experienced mixing between multiple fluid reservoirs (Marschall et al., 2006, 2008). Sulfur abundances and isotopic compositions in serpentinites, mica-schists, and metabasic samples have also been interpreted as indicative of the interaction of fluids from multiple sources in the Syros mélangé (Schwarzenbach et al., 2018).

Calcite is observed to overgrow glaucophane and epidote (Figures 2e and 2f) in thin section, implying that the late-stage fluids infiltrating 14HSY-35E were also C-bearing. This is consistent with field observations in which late-stage carbonate veins cross-cut high-pressure lithologies throughout Syros. Previous studies have concluded that fluid-mediated carbon liberation, in which aqueous fluids react with carbonate-rich lithologies (e.g., marble lithologies on Syros), is likely responsible for much of the carbon mobilization in subduction zones (Ague & Nicolescu, 2014; Gorce et al., 2018; Gorman et al., 2006; Kerrick & Connolly, 2001a, 2001b). Previously published thermodynamic constraints suggest that glaucophane-bearing marbles on Syros equilibrated with fluids with X_{CO_2} as low as 0.01 (Schumacher et al., 2008).

Exposure of sample 14HSY-35E to C-bearing fluids late in its history might explain the major discrepancies between the results presented in Figure 5 and the modal mineral abundances observed in this sample. Thin section observations suggest the breakdown of epidote and late-stage growth of dolomite (Figure 2f). While glaucophane overgrows high-pressure minerals such as omphacite (Figure 2b), there is also evidence of

dolomite replacing amphibole (Figure 2e), which could be interpreted as either dolomite growing at the expense of amphibole or late-stage fracture filling.

7.4. Implications of Compositional Zoning in Garnet

Based on Sm-Nd garnet ages and P - T calculations, it is likely that garnet compositional zoning in 14HSY-35E is representative of its early exhumation history. Detailed analyses of garnets in sample 14HSY-35E allow us to constrain heating and decompression rates. These results are of particular value because Sm-Nd geochronology for garnet core and rim populations is derived from the same garnets that were used to calculate P - T conditions of metamorphism. Thus, pressure, temperature, and geochronological data all obtained from a single sample were combined to constrain the P - T - t history of CBU lithologies on Syros.

Garnet core and rim growth stages are separated by 4.8 ± 2.1 Myr. We cannot constrain whether each stage of garnet growth occurred rapidly in a short pulse (<1 Myr as in Dragovic et al., 2012) or if garnet grew gradually and continuously over this entire period of time. Due to our sampling for geochronology (Figure 3) the core age will be dominated by inner core material (due to drill trench loss of outer core), and the rim age will be dominated by outer rim material (due to radial symmetry).

We suggest that the ~ 3 – 7 Myr timescale does not support extremely rapid mineral growth following a build-up of free energy due to overstepping for the second period of garnet growth. Furthermore, this timescale is significantly longer than those reported in studies that interpret oscillatory zoning within crystals to be the result of subtle pressure fluctuations (e.g., Beltrando et al., 2007; Garcia-Casco et al., 2002; Lister & Forster, 2016; Rubatto et al., 2011; Viete et al., 2018). Coupling estimated temperature conditions for garnet growth with garnet geochronology enables calculating of heating rates during Cycladic subduction. Phase equilibria modeling estimates that early garnet growth occurred over a temperature increase of $75 \pm 70^\circ\text{C}$ (assuming a temperature uncertainty of $\pm 50^\circ\text{C}$). Coupling this ΔT with the calculated garnet growth duration (along with propagating the associated uncertainties determined by Monte Carlo simulations ($n = 500$) using ranges of ΔT and Δt ; Dragovic et al., 2020) results in a heating rate of $15.6^\circ(+21.9/-14.8)^\circ\text{C}/\text{Myr}$, which is within uncertainty of the $22.3 \pm 8.0^\circ\text{C}/\text{Myr}$ reported by Dragovic et al. (2012, 2015) for CBU lithologies from the neighboring island of Sifnos. Such rapid isobaric heating has been predicted by geodynamic models (e.g., Syracuse et al., 2010) and previously attributed to either initial stages of exhumation while still in the subduction channel or to the presence of sharp thermal gradients as a consequence of slab-mantle coupling (Dragovic et al., 2015). Thermodynamic modeling and Sm-Nd garnet geochronology from this study yield decompression rates in the range ~ 0.3 – 0.7 cm/yr.

The mechanisms of decompression and exhumation of the CBU on Syros remain contentious. Since the geometry of the P - T path coupled with Sm-Nd garnet ages (Figure 9a) implies that oscillatory zoning in the garnets records the early exhumation history of 14HSY-35E (Figure 9), we can use these results to infer an exhumation mechanism for Syros terrains. In some studies, exhumation is thought to have occurred along the subduction channel. In this scenario, channel flow occurs within the serpentinite that forms along the slab-mantle interface (e.g., Gerya et al., 2002; Hermann et al., 2000). Extensive documentation of the Kampos unit on Syros (e.g., Bebout, 2007; Bebout & Barton, 2002; Breeding et al., 2004; Cloos & Shreve, 1988; Keiter et al., 2004; Spandler et al., 2008) supports this hypothesis. Channel flow can be simply driven by buoyancy differences between serpentinite and the dense mantle (e.g., Schwartz et al., 2001) or can be more complicated and involve forced channel flow (e.g., Herbert et al., 2009) or complex channel flow (e.g., Blanco-Quintero et al., 2011; Gerya et al., 2002; Hermann et al., 2000; Li et al., 2016; Qian & Wei, 2016).

We initially hypothesized an ascent of 14HSY-35E driven solely by buoyancy using appropriate densities. Using a density of $\sim 3,032$ kg/m³ at 485°C and 2.2 GPa (extracted from thermodynamic models that produced Figure 5) for an average value of $2,650$ kg/m³ (Schwartz et al., 2001) for fully serpentinitized peridotite, exhumation would require a subduction channel of at least 7–15 km thick (Schwartz et al., 2001), depending on the assumed decoupling velocity. Though typical eclogite is denser than that calculated for sample 14HSY-35E (a more silicious composition), if we were to assume a maximum density contrast of 700 kg/m³, upward flow would only occur if the subduction channel is a minimum of 2–3 km wide. Outcrops of the Kampos unit on Syros are usually less than 1 km wide, suggesting that buoyancy-driven channel flow was not sufficient alone to drive exhumation, and that forced and/or complex channel flow is required to ex-

hume a rock with characteristics similar to sample 14HSY-35E. Furthermore, the decompression rates calculated here ($\sim 0.3\text{--}0.7$ cm/yr) are faster than typically expected for buoyancy-driven ascension along a serpentinite subduction channel (e.g., Agard et al., 2009; Guillot et al., 2009).

While there is a lack of a sufficiently thick *mélange* channel on Syros to support purely buoyancy-driven ascension (see discussion above), forced channel flow exhumation models could provide a partial explanation for the exhumation of the upper CBU *mélange* in northern Syros. Calculated exhumation rates of $\sim 0.3\text{--}0.7$ cm/yr are comparable with geodynamic modeling results of Gerya et al. (2002), in which they assume a moderate convergence rate of 30 km/Myr during subduction and predict the development of a planar or wedge-shaped subduction channel with moderate flow. Thus, if the sample studied here was from the northern Syros Kampos unit, one might argue that the multiple pulses of metamorphism recorded by garnet are indicative of complex channel flow. However, channel flow mechanisms are difficult to reconcile with the more cohesive lower units of the CBU, as found in southern Syros from where 14HSY-35E originates. Thus, other mechanisms of exhumation must be considered in this case.

Garnet core ages reported here (45.3 ± 1.0 Ma) coincide well with combined detailed structural studies of the CBU and Ar-Ar dating in white mica that correlate the initiation of slab rollback (Royden & Husson, 2006; Schellart, 2004) and subsequent decoupling of the CBU with blueschist-facies overprinting due to decompression at ~ 45 Ma (e.g., Laurent et al., 2018; Lister & Forster, 2016; Roche et al., 2016). These studies also hypothesized a thermal excursion at ~ 35 Ma and final exhumation from 25 to 9 Ma, and argued that the inverse metamorphic gradient observed on Syros is evidence that the CBU was exhumed as a series of distinct tectonic slices. It has previously been shown that inherited Ar can be trapped in mica in high pressure terrains, leading to an overestimation of age (Warren, Hanke, & Kelley, 2012; Warren, Kelley, Sherlock, & McDonald, 2012). This has led to suggestions that the youngest reported $^{40}\text{Ar}/^{39}\text{Ar}$ ages represent true high-pressure metamorphism in the CBU and that slab rollback was not important until regional extension began around 24–21 Ma (e.g., Ring et al., 2020).

Skelton et al. (2019) concluded that that CBU is a subduction-related nappe stack that is comprised of at least three metamorphic belts: (a) the structurally higher *mélange* ophiolites in N. Syros, (b) the more cohesive units located in S. Syros, such those located near Fabrika, and (c) the structural lower CBU units on Evia and Sifnos. Ring et al. (2020) extended this interpretation and proposed that metamorphism in the CBU was driven by continuous return-flow processes in a conveyor belt model in which an extrusion wedge provided the environment for the subduction and subsequent exhumation of multiple tectonic slices. They suggested that the short distances between shear indicators observed in SE Syros and the lack of an observable, systematic arrangement of conflicting shear indicators, is evidence for forced return flow within the subduction channel. Both Ring et al. (2020) and Skelton et al. (2019) emphasize the role of lithospheric shortening in the evolution of an Aegean extrusion wedge, which is consistent with synorogenic exhumation proposed by other works (e.g., Laurent et al., 2018; Roche et al., 2016).

Based on the studies described above, it is likely that multiple exhumation mechanisms drove ascent of the CBU on Syros. We speculate that the older, initial exhumation of the Kampos unit in N. Syros may have been dominantly driven by forced return flow within the subduction channel, and that exhumation of the younger, cohesive volcanic-sedimentary units in S. Syros initiated, was driven by slab rollback coupled with localized regional extension and synorogenic exhumation. In the case of sample 14HSY-35E, the sample location, and similarities with inferred garnet *P-T* growth conditions reported by Skelton et al. (2019; decompression from ~ 2 to ~ 1.6 GPa) suggest that it records exhumation of 1, the younger tectonic slices of the CBU present on Syros.

8. Conclusions

Metamorphic garnets record two distinct stages of growth during HP/LT metamorphism of the CBU on Syros, Greece, from 2.2 GPa and 485°C to 2.0 GPa and 530°C (inner core-outer core) and from 2.1 GPa and 560°C to 1.6 GPa and 550°C (inner rim-outer rim). Models are in agreement with inclusion barometry, implying mechanical and chemical equilibrium. Zoned garnet Sm-Nd geochronology yields an age of 45.3 ± 1.0 Ma (2σ ; MSWD = 1.02, $n = 7$) for the inner/outer core domain and an age of 40.5 ± 1.9 Ma (2σ ; MSWD = 0.99, $n = 5$) for the inner/outer rim domain. To our knowledge, sample 14HSY-35E represents the

first example of metamorphic pressure, temperature, and age constraints derived from a single phase within an individual sample on Syros. We suggest that the sample may record the exhumation of parts of the CBU on Syros as a series of tectonic slices beginning ~45 Ma, with decompression rates of ~0.3–0.7 cm/yr and cooling rates of ~10–28°C/Myr.

Data Availability Statement

Data sets for this research are available in Advances in Subduction Zone Processes (Gorce, 2018), located in VTechWorks, which contains Virginia Tech Electronic Theses and Dissertations (EDTs) at <http://hdl.handle.net/10919/83810> (<http://rightsstatements.org/vocab/InC/1.0/>).

Acknowledgments

The authors thank H. Brooks and E. Ramos for assistance in fieldwork associated with this study. M. Tappa, P. Starr, and K. Maneiro provided invaluable assistance in the isotope geochronology. K. Ashley and C. Farley are thanked for assistance in data collection for the quartz barometry. L. Fedele and B. Tracy are thanked for microprobe assistance. J. S. Gorce thanks the Metamorphic Processes Group at Virginia Tech for comments on earlier versions of this work. M. J. Caddick and E. F. Baxter gratefully acknowledge support from NSF awards EAR-1250497 and EAR-1250470.

References

- Agard, P., Yamato, P., Jolivet, L., & Burov, E. (2009). Exhumation of oceanic blueschists and eclogites in subduction zones: Timing and mechanisms. *Earth-Science Reviews*, 92(1–2), 53–79. <https://doi.org/10.1016/j.earscirev.2008.11.002>
- Ague, J. J., & Nicolescu, S. (2014). Carbon dioxide released from subduction zones by fluid-mediated reactions. *Nature Geosciences*, 7(5), 355–360. <https://doi.org/10.1038/ngeo2143>
- Angel, R. J., Mazzucchelli, M. L., Alvaro, M., & Nestola, F. (2017). EosFit-Pinc: A simple GUI for host-inclusion elastic thermobarometry. *American Mineralogist*, 102(9), 1957–1960. <https://doi.org/10.2138/am-2017-6190>
- Angel, R. J., Mazzucchelli, M. L., Alvaro, M., Nimis, P., & Nestola, F. (2014). Geobarometry from host-inclusion systems: The role of elastic relaxation. *American Mineralogist*, 99(10), 2146–2149. <https://doi.org/10.2138/am-2014-5047>
- Ashley, K. T., Caddick, M. J., Steele-MacInnis, M. J., Bodnar, R. J., & Dragovic, B. (2014). Geothermobarometric history of subduction recorded by quartz inclusions in garnet. *Geochemistry, Geophysics, Geosystems*, 15, 350–360. <https://doi.org/10.1002/2013GC005106>
- Auzanneau, E., Schmidt, M. W., Vielzeuf, D., & Connolly, J. A. D. (2009). Titanium in phengite: A geobarometer for high temperature eclogites. *Contributions to Mineralogy and Petrology*, 159, 1–24. <https://doi.org/10.1007/s00410-009-0412-7>
- Baxter, E. F., Caddick, M. J., & Dragovic, B. (2017). Garnet: A rock-forming mineral petrochronometer. *Reviews in Mineralogy and Geochemistry*, 83(1), 469–533. <https://doi.org/10.2138/rmg.2017.83.15>
- Bebout, G. E. (1991). Field-based evidence for devolatilization in subduction zones: Implications for arc magmatism. *Science*, 251, 413–416. <https://doi.org/10.1126/science.251.4992.413>
- Bebout, G. E. (1995). The impact of subduction-zone metamorphism on mantle-ocean chemical cycling. *Chemical Geology*, 126(2), 191–218. [https://doi.org/10.1016/0009-2541\(95\)00118-5](https://doi.org/10.1016/0009-2541(95)00118-5)
- Bebout, G. E. (2007). Metamorphic chemical geodynamics of subduction zones. *Earth and Planetary Science Letters*, 206(3–4), 373–393. <https://doi.org/10.1016/j.epsl.2007.05.050>
- Bebout, G. E., & Barton, M. D. (2002). Tectonic and metasomatic mixing in a high-T, subduction-zone mélange—Insights into the geochemical evolution of the slab-mantle interface. *Chemical Geology*, 187(1–2), 79–106. [https://doi.org/10.1016/S0009-2541\(02\)00019-0](https://doi.org/10.1016/S0009-2541(02)00019-0)
- Behr, M. W., Kotowski, A. J., & Ashley, K. T. (2018). Dehydration-induced rheological heterogeneity and the deep tremor source in warm subduction zones. *Geology*, 46(5), 475–478. <https://doi.org/10.1130/G40105.1>
- Beltrando, M., Hermann, J., Lister, G., & Compagnoni, R. (2007). On the evolution of orogens: Pressure cycles and deformation mode switches. *Earth and Planetary Science Letters*, 256(3–4), 372–388. <https://doi.org/10.1016/j.epsl.2007.01.022>
- Berman, R. G. (1991). Thermobarometry using multi-equilibrium calculations; a new technique with petrological applications. *The Canadian Mineralogist*, 29(4), 833–855.
- Blanco-Quintero, I. F., García-Casco, A., & Gerya, T. V. (2011). Tectonic blocks in serpentinite mélange (eastern Cuba) reveal large-scale convective flow of the subduction channel. *Geology*, 39(1), 79–82. <https://doi.org/10.1130/G31494.1>
- Bonazzi, M., Tumiati, T., Thomas, J. B., Angel, R. J., & Alvaro, M. (2019). Assessment of the reliability of elastic geobarometry with quartz inclusions. *Lithos*, 350–351, 350–351. <https://doi.org/10.1016/j.lithos.2019.105201>
- Brady, J. B., Markley, M. J., Schumacher, J. C., Cheney, J. T., & Bianciardi, G. A. (2004). Aragonite pseudomorphs in high-pressure marbles of Syros, Greece. *Journal of Structural Geology*, 26(1), 3–9. [https://doi.org/10.1016/S0191-8141\(03\)00099-3](https://doi.org/10.1016/S0191-8141(03)00099-3)
- Breeding, C. M., Ague, J. J., & Bröcker, M. (2004). Fluid-metasedimentary rock interactions in subduction-zone mélange: Implications for the chemical composition of arc magmas. *Geology*, 32(12), 1041–1044. <https://doi.org/10.1130/G20877.1>
- Brockner, M., Bieling, D., Hacker, B., & Gans, P. (2013). High-Si phengite records the time of greenschist facies overprinting: Implications for models suggesting mega-detachments in the Aegean Sea. *Journal of Metamorphic Geology*, 22(5), 427–442. <https://doi.org/10.1111/j.1525-1314.2005.00524.x>
- Bröcker, M., & Enders, M. (2001). Unusual bulk-rock compositions in eclogite-facies rocks from Syros and Tinos (Cyclades, Greece): Implications for U-Pb zircon geochronology. *Chemical Geology*, 175(3–4), 581–603. [https://doi.org/10.1016/S0009-2541\(00\)00369-7](https://doi.org/10.1016/S0009-2541(00)00369-7)
- Bröcker, M., Kreuzer, H., Matthews, A., & Okrusch, M. (1993). ⁴⁰Ar/³⁹Ar and oxygen isotope studies of polymetamorphism from Tinos Island, Cycladic Blueschist Belt, Greece. *Journal of Metamorphic Geology*, 11(2), 223–240. <https://doi.org/10.1111/j.1525-1314.1993.tb00144.x>
- Brooks, H. L., Dragovic, B., Lamadrid, H. M., Caddick, M. J., & Bodnar, R. J. (2019). Fluid capture during exhumation of subducted lithologies: A fluid inclusion study from Sifnos, Greece. *Lithos*, 332–333, 120–134. <https://doi.org/10.1016/j.lithos.2019.01.014>
- Brun, J. P., & Faccenna, C. (2008). Exhumation of high-pressure rocks driven by slab rollback. *Earth and Planetary Science Letters*, 272(1–2), 1–7. <https://doi.org/10.1016/j.epsl.2008.02.038>
- Carlson, W. D., Patterson, D. R. M., & Caddick, M. J. (2015). Beyond the equilibrium paradigm: How consideration of kinetics enhances metamorphic interpretation. *American Mineralogist*, 100(8–9), 1659–1667. <https://doi.org/10.2138/am-2015-5097>
- Caron, J., & Pequignot, G. (1986). The transition between blueschists and lawsonite-bearing eclogites based on observations from Corsican metabasalts. *Lithos*, 19(3–4), 205–218. [https://doi.org/10.1016/0024-4937\(86\)90023-X](https://doi.org/10.1016/0024-4937(86)90023-X)
- Castro, A. E., & Spear, F. S. (2017). Reaction overstepping and re-evaluation of peak P-T conditions of the blueschist unit Sifnos, Greece: Implications for the Cyclades subduction zone. *International Geology Review*, 59(5–6), 548–562. <https://doi.org/10.1080/00206814.2016.1200499>

- Cisneros, M., Ashley, K. T., & Bodnar, R. J. (2020). Evaluation and application of the quartz-inclusions-in-epidote mineral barometer. *American Mineralogist*, 105(8), 1140–1151. <https://doi.org/10.2138/am-2020-7379>
- Cliff, R. A., Bond, C. E., Bulter, R. W. H., & Dixon, J. E. (2017). Geochronological challenges posed by continuously developing tectonometamorphic systems: Insights from Rb-Sr mica ages from the Cycladic Blueschist Belt, Syros (Greece). *Journal of Metamorphic Geology*, 35(2), 197–211. <https://doi.org/10.1111/jmg.12228>
- Cloos, M. (1982). Flow mélanges: Numerical modeling and geologic constraints on their origin in the Franciscan subduction complex, California. *The Geological Society of America Bulletin*, 93(4), 330–345. [https://doi.org/10.1130/0016-7606\(1982\)93<330:FMNMG>2.0.CO;2](https://doi.org/10.1130/0016-7606(1982)93<330:FMNMG>2.0.CO;2)
- Cloos, M., & Shreve, R. L. (1988). Subduction-channel model of prism accretion, mélange formation, sediment subduction, and subduction erosion at convergent plate margins: 2. Implications and discussion. *Pure and Applied Geophysics*, 128, 501–545. <https://doi.org/10.1007/BF00874549>
- Coggon, R., & Holland, T. J. B. (2002). Mixing properties of phengitic micas and revised garnet-phengite thermobarometers. *Journal of Metamorphic Geology*, 20(7), 683–696. <https://doi.org/10.1046/j.1525-1314.2002.00395.x>
- Connolly, J. A. D. (2005). Computation of phase equilibria by linear programming: A tool for geodynamic modeling and its application to subduction zone decarbonation. *Earth and Planetary Science Letters*, 236(1–2), 524–541. <https://doi.org/10.1016/j.epsl.2005.04.033>
- Cooperdock, E. H. G., Raia, N. H., Barnes, J. D., Stockli, D. F., & Schwarzenbach, E. M. (2018). Tectonic origin of serpentinites on Syros, Greece: Geochemical signatures of abyssal origin preserved in a HP/LT subduction complex. *Lithos*, 296–299, 352–364. <https://doi.org/10.1016/j.lithos.2017.10.020>
- Deiner, J. F. A., & Powell, R. (2012). Revised activity-composition models for clinopyroxene and amphibole. *Journal of Metamorphic Geology*, 30(2), 131–142. <https://doi.org/10.1111/j.1525-1314.2011.00959.x>
- Deiner, J. F. A., Powell, R., & White, R. W. (2008). Quantitative phase petrology of cordierite-orthoamphibole gneisses and related rocks. *Journal of Metamorphic Geology*, 26(8), 795–814. <https://doi.org/10.1111/j.1525-1314.2008.00791.x>
- Deiner, J. F. A., Powell, R., White, R. W., & Holland, T. J. B. (2007). A new thermodynamic model for clino- and orthoamphiboles in the system Na₂O-CaO-FeO-MgO-Al₂O₃-SiO₂-H₂O-O. *Journal of Metamorphic Geology*, 25(6), 631–656. <https://doi.org/10.1111/j.1525-1314.2007.00720.x>
- Dixon, J. E. (1976). Glauconite schists of Syros, Greece. *Bulletin de la Societe Geologique de France*, 18, 280. <https://doi.org/10.2113/gssgfbull.s7-xviii.2.280>
- Dixon, J. E., Feenstra, A., Jansen, J. B. H., Kreulen, R., Ridley, J., Salemink, J., & Schuiling, R. D. (1987). Excursion guide to the field trip on Seriphos, Syros, and Naxos. *Chemical Transport in Metasomatic Processes*, 218, 467–518. https://doi.org/10.1007/978-94-009-4013-0_18
- Dragovic, B., Angiboust, S., & Tappa, M. J. (2020). Petrochronological close-up on the thermal structure of a paleo-subduction zone (W. Alps). *Earth and Planetary Science Letters*, 547, 116446. <https://doi.org/10.1016/j.epsl.2020.116446>
- Dragovic, B., Baxter, E. F., & Caddick, M. J. (2015). Pulsed dehydration and garnet growth during subduction revealed by zoned garnet geochronology and thermodynamic modeling, Sifnos, Greece. *Earth and Planetary Science Letters*, 413, 111–122. <https://doi.org/10.1016/j.epsl.2014.12.024>
- Dragovic, B., Samanta, L. M., Baxter, E. F., & Selverstone, J. (2012). Using garnet to constrain the duration and rate of water-releasing metamorphic reactions during subduction: An example from Sifnos, Greece. *Chemical Geology*, 314–317, 9–22. <https://doi.org/10.1016/j.chemgeo.2012.04.016>
- Duisterhoeft, E., Quinteros, J., Oberhansli, R., Bousquet, R., & de Capitani, C. (2014). Relative impact of mantle densification and eclogitization of slabs on subduction dynamics: A numerical thermodynamic/thermokinematic investigation of metamorphic density evolution. *Tectonophysics*, 637, 20–29. <https://doi.org/10.1016/j.tecto.2014.09.009>
- Durr, S., Altherr, R., Keller, J., Okrusch, & M., & Seidel, E. (1978). The median Aegean crystalline belt: Stratigraphy, structure, metamorphism, magmatism. In *Alps, Apennines, Hellenides, Scientific Report* (pp. 455–477). Union Commission on Geodynamics.
- Enami, M., Nishiyama, T., & Mouri, T. (2007). Laser Raman microspectrometry of metamorphic quartz: A simple method for comparison of metamorphic pressures. *American Mineralogist*, 92(8–9), 1303–1315. <https://doi.org/10.2138/am.2007.2438>
- Federico, L., Crispini, L., Scambelluri, M., & Capponi, G. (2007). Ophiolite mélange zone records exhumation in a fossil subduction channel. *Geology*, 35(6), 499–502. <https://doi.org/10.1130/G23190A.1>
- Forster, M. A., & Lister, G. S. (2004). The interpretation of ⁴⁰Ar/³⁹Ar apparent age spectra produced by mixing: Application of the method of asymptotes and limits. *Journal of Structural Geology*, 26(2), 287–305. <https://doi.org/10.1016/j.jsg.2003.10.004>
- Forster, M. A., & Lister, G. S. (2005). Several distinct tectono-metamorphic slices in the Cycladic eclogite-blueschist belt, Greece. *Contributions to Mineral Petrology*, 150, 523–545. <https://doi.org/10.1007/s00410-005-0032-9>
- Fuhrman, M. L., & Lindsley, D. H. (1988). Ternary-feldspar modeling and thermometry. *American Mineralogist*, 73(3–4), 201–215.
- García-Casco, A., Torres-Roldán, R. L., Millán, G., Monie, P., & Schneider, J. (2002). Oscillatory zoning in eclogitic garnet and amphibole, Northern Serpentine Melange, Cuba: A record of tectonic instability during subduction. *Journal of Metamorphic Geology*, 20(6), 581–598. <https://doi.org/10.1046/j.1525-1314.2002.00390.x>
- Gatewood, M. P., Dragovic, B., Stowell, H. H., Baxter, E. F., Hirsch, D. M., & Bloom, R. (2015). Evaluating chemical equilibrium in metamorphic rocks using major element and Sm-Nd isotopic age zoning in garnet, Townshend Dam, Vermont, USA. *Chemical Geology*, 401, 151–168. <https://doi.org/10.1016/j.chemgeo.2015.02.017>
- Gerya, T. V., Stöckhert, B., & Perchuk, A. L. (2002). Exhumation of high-pressure metamorphic rocks in a subduction channel: A numerical simulation. *Tectonics*, 21(6), 6–1–6–19. <https://doi.org/10.1029/2002TC001406>
- Gorce, J. S. (2018). *Advances in subduction zone processes (Doctoral dissertation)*. Virginia Tech. Retrieved from <http://hdl.handle.net/10919/83810>
- Gorce, J. S., Caddick, M. J., & Bodnar, R. J. (2018). Thermodynamic constraints on carbonate breakdown and carbon volatile emission during subduction. *Earth and Planetary Science Letters*, 519, 213–222. <https://doi.org/10.1016/j.epsl.2019.04.047>
- Gorman, P. J., Kerrick, D. M., & Connolly, J. A. D. (2006). Modeling open system metamorphic decarbonation of subducting slabs. *Geochemistry, Geophysics, Geosystems*, 7(4). <https://doi.org/10.1029/2005GC001125>
- Green, E., Holland, T., & Powell, R. (2007). An order-disorder model for omphacitic pyroxenes in the system jadeite-diopside-hedenbergite-aemite, with applications to eclogitic rocks. *American Mineralogist*, 92(7), 1181–1189. <https://doi.org/10.2138/am.2007.2401>
- Guillot, S., Hattori, K., Agard, P., Schwartz, S., & Vidal, O. (2009). Exhumation processes in oceanic and continental subduction contexts: A review. In S. Lallemand, & F. Funiello (Eds.), *Subduction zone geodynamics. Frontiers in earth sciences* (pp. 175–205). Berlin, Heidelberg: Springer. https://doi.org/10.1007/978-3-540-87974-9_10
- Gyomlai, T., Agard, P., Marschall, H. R., Jolivet, L., & Gerdes, A. (2021). Metasomatism and deformation of block-in-matrix structures in Syros: The role of inheritance and fluid-rock interactions along the subduction interface. *Lithos*, 386–387, 386–387. <https://doi.org/10.1016/j.lithos.2021.105996>

- Hacker, B. R., Peacock, S. M., Abers, G. A., & Holloway, S. D. (2003). Subduction factory 2. Are intermediate-depth earthquakes in subducting slabs linked to metamorphic dehydration reactions? *Journal of Geophysical Research*, 108(B1). <https://doi.org/10.1029/2001JB001129>
- Hamelin, C., Brady, J. B., Cheney, J. T., Schumacher, J. C., Able, L. M., & Sperry, A. J. (2018). Pseudomorphs after Lawsonite from Syros, Greece. *Journal of Petrology*, 59(12), 2353–2384. <https://doi.org/10.1093/ptrology/egy099>
- Harvey, J., & Baxter, E. F. (2009). An improved method for TIMS high precision neodymium isotope analysis of very small aliquots (1–10 ng). *Chemical Geology*, 258(3–4), 251–257. <https://doi.org/10.1016/j.chemgeo.2008.10.024>
- Herbert, L. B., Antoshechkina, P., Asimow, P., & Gurnis, M. (2009). Emergence of a low-viscosity channel in subduction zones through the coupling of mantle flow and thermodynamics. *Earth and Planetary Science Letters*, 278(3–4), 243–256. <https://doi.org/10.1016/j.epsl.2008.12.013>
- Hermann, J., Müntener, O., & Scambelluri, M. (2000). The importance of serpentinite mylonites for subduction and exhumation of oceanic crust. *Tectonophysics*, 327(3–4), 225–238. [https://doi.org/10.1016/S0040-1951\(00\)00171-2](https://doi.org/10.1016/S0040-1951(00)00171-2)
- Holland, T. J. B., & Powell, R. (1991). A compensated-Redlich-Kwong (CORK) equation for volumes and fugacities of CO₂ and H₂O in the range 1 bar to 50 kbar and 100–1600°C. *Contributions to Mineralogy and Petrology*, 109(2), 265–273. <https://doi.org/10.1007/BF00306484>
- Holland, T. J. B., & Powell, R. (1998). An internally consistent thermodynamic data set for phases of petrological interest. *Journal of Metamorphic Geology*, 16(3), 309–343. <https://doi.org/10.1111/j.1525-1314.1998.00140.x>
- Hoschek, G. (2013). Garnet zonation in metapelitic schists from the Eclogite Zone, Tauern Window, Austria: Comparison of observed and calculated profiles. *European Journal of Mineralogy*, 25(4), 615–629. <https://doi.org/10.1127/0935-1221/2013/0025-2310>
- Husson, L., Brun, J. P., Yamato, P., & Faccenna, C. (2009). Episodic slab rollback fosters exhumation of HP–UHP rocks. *Geophysical Journal International*, 179(3), 1292–1300. <https://doi.org/10.1111/j.1365-246X.2009.04372.x>
- Jones, G., & Robertson, A. H. F. (1991). Stratigraphy and evolution of the Mesozoic Pindos ophiolite and related units, northwest Greece. *Journal of the Geologic Society of London*, 148, 267–288. <https://doi.org/10.1144/gsjgs.148.2.0267>
- Keay, S. (1998). *The geological evolution of the Cyclades, Greece: Constraints from SHRIMP U-Pb geochronology* (p. 335). Canberra, ACT: Department of Geology, Australian National University. <https://doi.org/10.25911/5d46671ad2b2f>
- Keiter, M., Ballhaus, C., & Tomaschek, F. (2011). *A new geological map of the Island of Syros (Aegean Sea, Greece): Implications for lithostratigraphy and structural history of the Cycladic Blueschist Unit (Special Paper)* (Vol. 481, pp. 1–43). Geological Society of America. <https://doi.org/10.1130/2011.2481>
- Keiter, M., Piepjohn, K., Ballhaus, C., Lagos, M., & Bode, M. (2004). Structural development of high-pressure metamorphic rocks on Syros island (Cyclades, Greece). *Journal of Structural Geology*, 26(8), 1433–1445. <https://doi.org/10.1016/j.jsg.2003.11.027>
- Kerrick, D. M., & Connolly, J. A. D. (2001a). Metamorphic devolatilization of subducted marine sediments and the transport of volatiles into the Earth's mantle. *Nature*, 411, 293–296. <https://doi.org/10.1038/35077056>
- Kerrick, D. M., & Connolly, J. A. D. (2001b). Metamorphic devolatilization of subducted oceanic metabasalts: Implications for seismicity, arc magmatism and volatile recycling. *Earth and Planetary Science Letters*, 189(1–2), 19–29. [https://doi.org/10.1016/S0012-821X\(01\)00347-8](https://doi.org/10.1016/S0012-821X(01)00347-8)
- Kohn, M. J. (2009). Models of garnet differential geochronology. *Geochimica et Cosmochimica Acta*, 73(1), 170–182. <https://doi.org/10.1016/j.gca.2008.10.004>
- Kohn, M. J. (2014). “Thermobarometry-try”: Calibration of spectroscopic barometers and thermometers for mineral inclusions. *Earth and Planetary Science Letters*, 388, 187–196. <https://doi.org/10.1016/j.epsl.2013.11.054>
- Kotowski, A. J., & Behr, W. M. (2019). Length scales and types of heterogeneities along the deep subduction interface: Insights from exhumed rocks on Syros Island, Greece. *Geosphere*, 15(4), 1038–1065. <https://doi.org/10.1130/GES02037.1>
- Kouketsu, Y., Nishiyama, T., Ikeda, T., & Enami, M. (2014). Evaluation of residual pressure in an inclusion-host system using negative frequency shift of quartz Raman spectra. *American Mineralogist*, 99(2–3), 433–442. <https://doi.org/10.2138/am.2014.4427>
- Krohe, A., & Mposkos, E. (2002). Multiple generations of extensional detachments in the Rhodope Mountains (northern Greece): Evidence of episodic exhumation of high-pressure rocks. *Geological Society, London, Special Publications*, 204, 151–178. <https://doi.org/10.1144/GSL.SP.2002.204.01.10>
- Lagos, M., Scherer, E. E., Tomaschek, F., Münker, C., Keiter, M., Berndt, J., & Ballhaus, C. (2007). High precision Lu-Hf geochronology of Eocene eclogite-facies rocks from Syros, Cyclades, Greece. *Chemical Geology*, 243(1–2), 16–35. <https://doi.org/10.1016/j.chemgeo.2007.04.008>
- Laurent, V., Jolivet, L., Roche, V., Augier, R., Scaillet, S., & Cardello, L. (2016). Strain localization in a fossilized subduction channel: Insights from the Cycladic Blueschist Unit (Syros, Greece). *Tectonophysics*, 672–673, 150–169. <https://doi.org/10.1016/j.tecto.2016.01.036>
- Laurent, V., Lanari, P., Naïr, I., Augier, R., Lahfid, A., & Jolivet, L. (2018). Exhumation of eclogite and blueschist (Cyclades, Greece): Pressure-temperature evolution determined by thermobarometry and garnet equilibrium modelling. *Journal of Metamorphic Geology*, 36, 769–798. <https://doi.org/10.1111/jmg.1230>
- Li, J., Gao, J., Klemm, R., John, T., & Wang, X. (2016). Redox processes in subducting oceanic crust recorded by sulfide-bearing high-pressure rocks and veins (SW Tianshan, China). *Contributions to Mineralogy and Petrology*, 171, 72. <https://doi.org/10.1007/s00410-016-1284-2>
- Lips, A. L. W., White, S. H., & Wijbrans, J. R. (1998). ⁴⁰Ar/³⁹Ar laserprobe direct dating of discrete deformational events: A continuous record of early Alpine tectonics in the Pelagonian Zone, NW Aegean area, Greece. *Tectonophysics*, 298(1–3), 133–153. [https://doi.org/10.1016/S0040-1951\(98\)00181-4](https://doi.org/10.1016/S0040-1951(98)00181-4)
- Lister, G. S., & Forster, M. A. (2016). White mica ⁴⁰Ar/³⁹Ar age spectra and the timing of multiple episodes of high-pressure metamorphic mineral growth in the Cycladic eclogite-blueschist belt, Syros, Aegean Sea, Greece. *Journal of Metamorphic Geology*, 34(5), 401–421. <https://doi.org/10.1111/jmg.12178>
- Lister, G. S., & Raouzaïos, A. (1996). The tectonic significance of a porphyroblastic blueschist facies overprint during Alpine orogenesis: Sifnos, Aegean Sea, Greece. *Journal of Structural Geology*, 18(12), 1417–1435. [https://doi.org/10.1016/S0191-8141\(96\)00072-7](https://doi.org/10.1016/S0191-8141(96)00072-7)
- Maluski, H., Bonneau, M., & Kienast, J. R. (1987). Dating the metamorphic events in the Cycladic area; ³⁹Ar/⁴⁰Ar data from metamorphic rocks of the Island of Syros (Greece). *Bulletin de la Société Géologique de France*, 3(5), 833–842. <https://doi.org/10.2113/gssgfbull.III.5.833>
- Marmo, B. A., Clarke, G. L., & Powell, R. (2002). Fractionation of bulk rock composition due to porphyroblast growth; effects on eclogite facies mineral equilibria, Pam Peninsula, New Caledonia. *Journal of Metamorphic Geology*, 20, 51–165. <https://doi.org/10.1046/j.0263-4929.2001.00346.x>
- Marschall, H. R., Altherr, R., Kalt, A., & Ludwig, T. (2008). Detrital, metamorphic and metasomatic tourmaline in high-pressure meta-sediments from Syros (Greece): Intra-grain boron isotope patterns determined by secondary-ion mass spectroscopy. *Contributions to Mineralogy and Petrology*, 155, 703–717. <https://doi.org/10.1007/s00410-007-0266-9>
- Marschall, H. R., Altherr, R., Ludwig, T., Kalt, A., Gmeling, K., & Kasztovszky, Z. (2006). Partitioning and budget of Li, Be, and B in high-pressure metamorphic rocks. *Geochimica et Cosmochimica Acta*, 70(18), 4750–4769. <https://doi.org/10.1016/j.gca.2006.07.006>

- Marschall, H. R., & Schumacher, J. C. (2012). Arc magma sourced from mélange diapirs in subduction zones. *Nature Geoscience*, 5, 862–867. <https://doi.org/10.1038/ngeo1634>
- Maruyama, S., Liou, J. G., & Terabayashi, M. (1996). Blueschists and eclogites of the world and their exhumation. *International Geology Review*, 38(6), 485–594. <https://doi.org/10.1080/00206819709465347>
- Matthews, A., & Schliestedt, M. (1984). Evolution of the blueschist and greenschist facies rocks of Sifnos, Cyclades, Greece. *Contributions to Mineralogy and Petrology*, 88, 150–163. <https://doi.org/10.1007/BF00371419>
- Milani, S., Nestola, F., Alvaro, M., Pasqual, D., Mazzucchelli, M. L., Domeneghetti, M. C., & Geiger, C. A. (2015). Diamond-garnet geobarometry: The role of garnet compressibility and expansivity. *Lithos*, 227, 140–147. <https://doi.org/10.1016/j.lithos.2015.03.017>
- Mposkos, E. D., & Kostopoulos, D. K. (2001). Diamond, former coesite and supersilicic garnet in metasedimentary rocks from the Greek Rhodope: A new ultrahigh-pressure metamorphic province established. *Earth and Planetary Science Letters*, 192(4), 497–506. [https://doi.org/10.1016/S0012-821X\(01\)00478-2](https://doi.org/10.1016/S0012-821X(01)00478-2)
- Neilsen, S. G., & Marschall, H. R. (2017). Geochemical evidence for mélange melting in global arcs. *Science Advances*, 3(4), e1602402. <https://doi.org/10.1126/sciadv.1602402>
- Okrusch, M., & Broecker, M. (1990). Eclogites associated with high-grade blueschists in the Cyclades archipelago, Greece: A review. *European Journal of Mineralogy*, 2(4), 451–478. <https://doi.org/10.1127/ejm/2/4/0451>
- Palin, R. M., Weller, O. M., Waters, D. J., & Dyck, B. (2016). Quantifying geological uncertainty in metamorphic phase equilibria modelling: a Monte Carlo assessment and implications for tectonic interpretations. *Geoscience Frontiers*, 7(4), 591–607. <https://doi.org/10.1016/j.gsf.2015.08.005>
- Peacock, S. M. (1993). The importance of blueschist→ eclogite dehydration reactions in subducting oceanic crust. *The Geological Society of America Bulletin*, 105, 684–694. [https://doi.org/10.1130/0016-7606\(1993\)105<0684:TIOBED>2.3.CO;2](https://doi.org/10.1130/0016-7606(1993)105<0684:TIOBED>2.3.CO;2)
- Peacock, S. M. (2004). Thermal structure and metamorphic evolution of subducting slabs. In J. Eiler (Ed.), *Inside the subduction factory* (pp. 7–22). American Geophysical Union. <https://doi.org/10.1029/138GM02>
- Penniston-Dorland, S. C., Sorensen, S. S., Ash, R. D., & Khadke, S. V. (2010). Lithium isotopes as a tracer of fluids in a subduction zone mélange: Franciscan Complex, CA. *Earth and Planetary Science Letters*, 292(1–2), 181–190. <https://doi.org/10.1016/j.epsl.2010.01.034>
- Philippou, M., Brun, J., & Gueydan, F. (2011). Tectonics of the Syros blueschists (Cyclades, Greece): From subduction to Aegean extension. *Tectonics*, 30(4), TC4001. <https://doi.org/10.1029/2010TC002810>
- Philippou, M., Gueydan, F., Pitra, P., & Brun, J. (2013). Preservation of subduction-related prograde deformation in lawsonite pseudomorph-bearing rocks. *Journal of Metamorphic Geology*, 31(5), 571–583. <https://doi.org/10.1111/jmg.12035>
- Pollington, A. D., & Baxter, E. F. (2011). High precision microsampling and preparation of zoned garnet porphyroblasts for Sm–Nd geochronology. *Chemical Geology*, 281(3–4), 270–282. <https://doi.org/10.1016/j.chemgeo.2010.12.014>
- Putlitz, B., Cosca, M. A., & Schumacher, J. C. (2005). Prograde mica ⁴⁰Ar/³⁹Ar growth ages recorded in high pressure rocks (Syros, Cyclades, Greece). *Chemical Geology*, 214(1–2), 79–98. <https://doi.org/10.1016/j.chemgeo.2004.08.056>
- Qian, J. H., & Wei, C. J. (2016). P–T–t evolution of garnet amphibolites in the Wutai-Hengshan area, North China Craton: Insights from phase equilibria and geochronology. *Journal of Metamorphic Geology*, 34(5), 423–446. <https://doi.org/10.1111/jmg.12186>
- Ridley, J. (1984). *The significance of deformation associated with blueschist facies metamorphism on the Aegean Island of Syros* (Vol. 17, pp. 545–550). Geological Society of London Special Publication. <https://doi.org/10.1144/GSL.SP.1984.017.01.41>
- Ring, U., Glodny, J., Will, T., & Thomson, S. (2010). The Hellenic subduction system: High-pressure metamorphism, exhumation, normal faulting, and large-scale extension. *Annual Review of Earth and Planetary Sciences*, 38(1), 45–76. <https://doi.org/10.1146/annurev.earth.050708.170910>
- Ring, U., & Layer, P. W. (2003). High-pressure metamorphism in the Aegean, eastern Mediterranean: Underplating and exhumation from the Late Cretaceous until the Miocene to Recent above the retreating Hellenic subduction zone. *Tectonics*, 22(3), 1022. <https://doi.org/10.1029/2001TC001350>
- Ring, U., Pantazides, H., Glodny, J., & Skelton, A. (2020). Forced return flow deep in the subduction channel, Syros, Greece. *Tectonics*, 39, e2019TC005768. <https://doi.org/10.1029/2019TC005768>
- Roche, V., Laurent, V., Cardello, G. L., Jolivet, L., & Scaillet, S. (2016). Anatomy of the Cycladic Blueschist Unit on Sifnos Island (Cyclades, Greece). *Journal of Geophysics*, 97, 62–87. <https://doi.org/10.1016/j.jog.2016.03.008>
- Rosenbaum, G., Avigad, D., & Sánchez-Gómez, M. (2002). Coaxial flattening at deep levels of orogenic belts: Evidence from blueschists and eclogites on Syros and Sifnos (Cyclades, Greece). *Journal of Structural Geology*, 24(9), 1451–1462. [https://doi.org/10.1016/S0191-8141\(01\)00143-2](https://doi.org/10.1016/S0191-8141(01)00143-2)
- Royden, L. H., & Husson, L. (2006). Trench motion, slab geometry and viscous stresses in subduction systems. *Geophysical Journal International*, 167(2), 881–905. <https://doi.org/10.1111/j.1365-246X.2006.03079.x>
- Rubatto, D., Regis, D., Hermann, J., Boston, K., Engi, M., Beltrando, M., & McAlpine, S. R. B. (2011). Yo-yo subduction recorded by accessory minerals in the Italian Western Alps. *Nature Geoscience*, 4, 338–342. <https://doi.org/10.1038/ngeo1124>
- Schellart, W. P. (2004). Quantifying the net slab pull force as a driving mechanism for plate tectonics. *Geophysical Research Letters*, 31(7), L07611. <https://doi.org/10.1029/2004GL019528>
- Schmidt, C., & Ziemann, M. A. (2000). In-situ Raman spectroscopy of quartz: A pressure sensor for hydrothermal diamond-anvil cell experiments at elevated temperatures. *American Mineralogist*, 85(11–12), 1725–1734. <https://doi.org/10.2138/am-2000-11-1216>
- Schumacher, J. C., Brady, J. B., Cheney, J. T., & Tonnsen, R. R. (2008). Glaucophane-bearing marbles on Syros, Greece. *Journal of Petrology*, 49(9), 1667–1686. <https://doi.org/10.1093/petrology/egn042>
- Schwartz, S., Allemand, P., & Guillot, S. (2001). Numerical model of the effect of serpentinites on the exhumation of eclogitic rocks: Insights from the Monviso ophiolitic massif (Western Alps). *Tectonophysics*, 342(1–2), 193–206. [https://doi.org/10.1016/S0040-1951\(01\)00162-7](https://doi.org/10.1016/S0040-1951(01)00162-7)
- Schwarzenbach, E. M., Caddick, M. J., Petroff, M., Gill, B. C., Cooperdock, E. H. G., & Barnes, J. D. (2018). Sulphur and carbon cycling in the subduction zone mélange. *Scientific Reports*, 8, 15517. <https://doi.org/10.1038/s41598-018-33610-9>
- Sherlock, S., Kelley, S., Inger, S., Harris, N., & Okay, A. (1999). ⁴⁰Ar–³⁹Ar and Rb–Sr geochronology of high-pressure metamorphism and exhumation history of the Tavsanli Zone, NW Turkey. *Contributions to Mineralogy and Petrology*, 137(1–2), 46–58. <https://doi.org/10.1007/PL00013777>
- Skelton, A., Peilod, A., Glodny, J., Klonowska, I., Månbro, C., Lodin, K., & Ring, U. (2019). Preservation of high-P rocks coupled to rock composition and the absence of metamorphic fluids. *Journal of Metamorphic Geology*, 37, 359–381. <https://doi.org/10.1111/jmg.12466>
- Soukis, K., & Stockli, D. F. (2013). Structural and thermochronometric evidence for multi-stage exhumation of southern Syros, Cycladic, islands, Greece. *Tectonophysics*, 595–596, 148–164. <https://doi.org/10.1016/j.tecto.2012.05.017>

- Spandler, C., Hermann, J., Faure, K., Mavrogenes, J. A., & Arculus, R. J. (2008). The importance of talc and chlorite “hybrid” rocks for volatile recycling through subduction zones; evidence from the high-pressure subduction mélange of New Caledonia. *Contributions to Mineralogy and Petrology*, 155, 181–198. <https://doi.org/10.1007/s00410-007-0236-2>
- Spear, F. S. (2017). Garnet growth after overstepping. *Chemical Geology*, 466, 491–499. <https://doi.org/10.1016/j.chemgeo.2017.06.038>
- Spear, F. S., & Patterson, D. R. M. (2017). The implications of overstepping for metamorphic assemblage diagrams (MADs). *Chemical Geology*, 457, 38–46. <https://doi.org/10.1016/j.chemgeo.2017.03.011>
- Spear, F. S., Thomas, J. B., & Hallett, B. W. (2014). Overstepping the garnet isograd: A comparison of QuiG barometry and thermodynamic modeling. *Contributions to Mineralogy and Petrology*, 168, 1059. <https://doi.org/10.1007/s00410-014-1059-6>
- Spear, F. S., & Wolfe, O. M. (2019). Implications of overstepping of garnet nucleation for geothermometry, geobarometry and P-T path calculations. *Chemical Geology*, 530. <https://doi.org/10.1016/j.chemgeo.2019.11932310>
- Starr, P. G., Broadwell, K. S., Dragovic, B., Scambelluri, M., Haws, A. A., Caddick, M. J., et al. (2020). The subduction and exhumation history of the Voltri Ophiolite, Italy: Evaluating exhumation mechanisms for high-pressure metamorphic massifs. *Lithos*, 376–377, 105767. <https://doi.org/10.1016/j.lithos.2020.105767>
- Syracuse, E. M., van Keken, P. E., & Abers, G. A. (2010). The global range of subduction zone thermal models. *Physics of the Earth and Planetary Interiors*, 183(1–2), 73–90. <https://doi.org/10.1016/j.pepi.2010.02.004>
- Thomas, J. B., & Spear, F. S. (2018). Experimental study of quartz inclusions in garnet at pressures up to 3.0 GPa: Evaluating validity of the quartz-in-garnet inclusion elastic thermobarometer. *Contributions to Mineralogy and Petrology*, 173, 42. <https://doi.org/10.1007/s00410-018-1469-y>
- Tomaschek, F., Kennedy, A. K., Villa, I. M., Lagos, M., & Ballhaus, C. (2003). Zircon from Syros, Cyclades, Greece—Recrystallization and mobilization of zircon during high-pressure metamorphism. *Journal of Petrology*, 44(11), 1977–2002. <https://doi.org/10.1093/petrology/egg067>
- Tracy, R. J., Robinson, P., & Thompson, A. B. (1976). Garnet Composition and zoning in the determination of temperature and pressure of metamorphism, central Massachusetts. *American Mineralogist*, 61(7–8), 762–775.
- Tremblay, A., Meshi, A., Deschamps, T., Goulet, F., & Goulet, N. (2015). The Vardar zone as a suture for the Mirdita ophiolites, Albania: Constraints from the structural analysis of the Korabi-Pelagonia zone. *Tectonics*, 34, 352–375. <https://doi.org/10.1002/2014TC003807>
- Trotet, F., Jolivet, L., & Vidal, O. (2001). Tectono-metamorphic evolution of Syros and Sifnos islands (Cyclades, Greece). *Tectonophysics*, 338(2), 79–206. [https://doi.org/10.1016/S0040-1951\(01\)00138-X](https://doi.org/10.1016/S0040-1951(01)00138-X)
- Trotet, F., Vidal, O., & Jolivet, L. (2001). Exhumation of Syros and Sifnos metamorphic rocks (Cyclades, Greece). New constraints on the P-T paths. *European Journal of Mineralogy*, 13(5), 901–920. <https://doi.org/10.1127/0935-1221/2001/0013-0901>
- Uunk, B., Brouwer, F., ter Voorde, M., & Wijbrans, J. (2018). Understanding phengite argon closure using grain fusion age distributions in the Cycladic Blueschist Unit on Syros, Greece. *Earth and Planetary Science Letters*, 484, 192–203. <https://doi.org/10.1016/j.epsl.2017.12.031>
- Viete, D. R., Hacker, R. B., Allen, M. B., Seward, G. G., Tobin, M. J., Kelley, C. S., et al. (2018). Metamorphic records of multiple seismic cycles during subduction. *Science Advances*, 4(3), eaaq0234. <https://doi.org/10.1126/sciadv.aaq0234>
- Von Quadt, A., Moritz, R., Peytcheva, I., & Heinrich, C. A. (2005). Geochronology and geodynamics of Late Cretaceous magmatism and Cu-Au mineralization in the Panagyurishte region of the Apuseni-Banat-Timok-Srednogie belt, Bulgaria. *Ore Geology Reviews*, 27(1–4), 95–126. <https://doi.org/10.1016/j.oregeorev.2005.07.024>
- Warren, C. J., Hanke, F., & Kelley, S. P. (2012). When can muscovite ⁴⁰Ar/³⁹Ar dating constrain the timing of metamorphic exhumation? *Chemical Geology*, 291, 79–86. <https://doi.org/10.1016/j.chemgeo.2011.09.017>
- Warren, C. J., Kelley, S. P., Sherlock, S. C., & McDonald, C. S. (2012). Metamorphic rocks seek meaningful cooling rate: Interpreting ⁴⁰Ar/³⁹Ar ages in an exhumed ultra-high pressure terrane. *Lithos*, 155, 30–48. <https://doi.org/10.1016/j.lithos.2012.08.011>
- White, R. W., Pomroy, N. E., & Powell, R. (2005). An in situ metatexite-diatexite transition in upper amphibolite facies rocks from Broken Hill, Australia. *Journal of Metamorphic Geology*, 23(7), 579–602. <https://doi.org/10.1111/j.1525-1314.2005.00597.x>
- White, R. W., Powell, R., & Clarke, G. L. (2002). The interpretation of reaction textures in Fe-rich metapelitic granulites of the Musgrave Block, central Australia: Constraints from mineral equilibria calculations in the system K₂O-FeO-MgO-Al₂O₃-SiO₂-H₂O-TiO₂-Fe₂O₃. *Journal of Metamorphic Geology*, 20(1), 41–55. <https://doi.org/10.1046/j.0263-4929.2001.00349.x>
- Wolfe, O. M., & Spear, F. S. (2018). Determining the amount of overstepping required to nucleate garnet during Barrovian regional metamorphism. *Journal of Metamorphic Geology*, 36(1), 79–94. <https://doi.org/10.1111/jmg.12284>
- Zhang, Y. (1998). Mechanical and phase equilibria in inclusion-host systems. *Earth and Planetary Science Letters*, 57(3–4), 209–222. [https://doi.org/10.1016/S0012-821X\(98\)00036-3](https://doi.org/10.1016/S0012-821X(98)00036-3)
- Zhong, X., Moulas, E., & Tajčmanová, L. (2020). Post-entrapment modification of residual inclusion pressure and its implications for Ram elastic thermobarometry. *Solid Earth*, 11(1), 223–240. <https://doi.org/10.5194/se-11-223-2020>